AGU PUBLICATIONS

JGR

Journal of Geophysical Research: Oceans

RESEARCH ARTICLE

10.1002/2014JC009898

Key Points:
- Large transport was induced by Gulf Stream Warm Core Ring
- The nonlinear advection and JEBAR play important roles in eddy dynamics
- The Gulf Stream Ring has strong impact on coastal circulation

Correspondence to:
R. He,
rhe@ncsu.edu

Citation:
Chen, K., R. He, B. S. Powell, G. G. Gawarkiewicz, A. M. Moore, and H. G. Arango (2014), Data assimilative modeling investigation of Gulf Stream Warm Core Ring interaction with continental shelf and slope circulation, *J. Geophys. Res. Oceans*, *119*, doi:10.1002/2014JC009898.

Received 11 FEB 2014
Accepted 8 JUN 2014
Accepted article online 14 JUN 2014

Data assimilative modeling investigation of Gulf Stream Warm Core Ring interaction with continental shelf and slope circulation

Ke Chen[1], Ruoying He[2], Brian S. Powell[3], Glen G. Gawarkiewicz[1], Andrew M. Moore[4], and Hernan G. Arango[5]

[1]Department of Physical Oceanography, Woods Hole Oceanographic Institution, Woods Hole, Massachusetts, USA, [2]Department of Marine Earth and Atmospheric Sciences, North Carolina State University, Raleigh, North Carolina, USA, [3]Department of Oceanography, University of Hawaii at Manoa, Honolulu, Hawaii, USA, [4]Department of Ocean Sciences, University of California, Santa Cruz, California, USA, [5]Institute of Marine and Coastal Sciences, Rutgers University, New Brunswick, New Jersey, USA

Abstract A data assimilative ocean circulation model is used to hindcast the interaction between a large Gulf Stream Warm Core Ring (WCR) with the Mid-Atlantic Bight (MAB) shelf and slope circulation. Using the recently developed Incremental Strong constraint 4D Variational (I4D-Var) data assimilation algorithm, the model assimilates mapped satellite sea surface height (SSH), sea surface temperature (SST), in situ temperature, and salinity profiles measured by expendable bathythermograph, Argo floats, shipboard CTD casts, and glider transects. Model validations against independent hydrographic data show 60% and 57% error reductions in temperature and salinity, respectively. The WCR significantly changed MAB continental slope and shelf circulation. The mean cross-shelf transport induced by the WCR is estimated to be 0.28 Sv offshore, balancing the mean along-shelf transport by the shelfbreak jet. Large heat/salt fluxes with peak values of 8900 W m^{-2}/4 $\times$ 10^{-4} kg m^{-2} s^{-1} are found when the WCR was impinging upon the shelfbreak. Vorticity analysis reveals the nonlinear advection term, as well as the residual of joint effect of baroclinicity and bottom relief (JEBAR) and advection of potential vorticity (APV) play important roles in controlling the variability of the eddy vorticity.

1. Introduction

The Mid-Atlantic Bight and Gulf of Maine encompass the coastal region of the northeastern North America from Cape Hatteras to Nova Scotia. This region lies in the western boundary confluent zone, where the subpolar gyre and Labrador current/Scotia shelf waters move south, and the subtropical gyre and the Gulf Stream move north [*Loder et al.*, 1998]. These currents and water masses interact at various spatial and temporal scales, and together constitute a unique setting for studying a range of important shelf-deep ocean interactions processes. Annual mean shelf transport estimated by *Loder et al.* [1998] shows that there is a systematic reduction in the alongshore transport, varying roughly from 7.5 Sv in the Labrador Sea to 0.7 Sv off Nova Scotia. There are further transport reductions as the Scotian shelf and slope waters enter the Gulf of Maine (GOM), and subsequently move into the Middle Atlantic Bight (MAB). Such equatorward transport is accompanied by complex cross-shelf exchange processes between the shelf water and the Slope Sea. Several processes have been identified but the most energetic one is the Gulf Stream Warm Core Ring (WCR, hereafter) interactions with the shelf/slope waters. For example, *Joyce et al.* [1992] indicate that a single ring acting near the MAB shelfbreak over a short time span (a couple of months) can account for the entire shelf-ocean transport and flux exchange over a year.

Earlier studies on WCRs and their related cross-shelf exchange processes were based on in situ data combined with available satellite observations [e.g., *Morgan and Bishop*, 1977; *Bisagni*, 1983; *Joyce*, 1984; *Churchill et al.*, 1986; *Houghton et al.*, 1986; *Garfield and Evans*, 1987]. They have provided important insight into WCR dynamics and estimates of cross-shelf transport and fluxes based on available observations. More recently, *Pickart et al.* [1999] by using ship hydrography, acoustic Doppler current profiler (ADCP) data and satellite imagery, revealed the spatial pattern of a shelfbreak meander associated with a Gulf Stream WCR. Similarly, *Gawarkiewicz et al.* [2001] focused on the influence of a slope eddy on the shelfbreak frontal jet

and provided a generalized schematic of the eddy-jet interaction process. Using long time series of satellite-derived sea surface temperature data and estimates of (a constant) vertical scale for the shelf water within the streamers, *Chaudhuri et al*. [2008] analyzed interannual variability of WCRs and produced estimates of shelf water entrainment. A number of modeling analyses have been conducted to address various dynamical aspects associated with WCRs. *Chapman and Brink* [1987] used a linear model to delineate the dynamics of an offshore eddy impinging upon a stratified shelf and slope. *Wang* [1992] applied a 3-dimensional nonlinear model to describe the evolution of cyclonic eddies and shelf/slope response. *Wei and Wang* [2009] used the Princeton Ocean Model to simulate the interaction of a Warm Core Ring with continental shelf and slope bathymetry in the Mid-Atlantic Bight by using quasi-realistic topography.

Indeed, understanding the detailed WCRs dynamics has been a long-standing research topic. With the presence of the shelfbreak front and jet [*Gawarkiewicz et al*., 1996, 2001; *Linder and Gawarkiewicz*, 1998; *Fratantoni et al*., 2001; *Chen and He*, 2010] steep topography, and large baroclinic gradients in the MAB, the WCR-induced exchange at the shelfbreak is highly complex and nonlinear, posing a great challenge to simulate it. While the model can typically get the general pattern of the WCR correct, mismatches in exact ring location and intensity between the model and observation exist. The recently developed Incremental Strong constraint 4D-Variational (I4D-Var) data assimilation algorithm [*Moore et al*., 2011a, 2011b, 2011c] for ROMS allows observations to be dynamically ingested into the model, representing a major step forward in modeling complex hydrodynamic features like WCRs. In this study, we investigate the shelf circulation and the shelf/slope exchange processes during a Warm Core Ring event occurred in spring 2006, which is one of the most energetic WCRs observed in the last decade. In situ and remote sensing observations are assimilated using I4D-Var into a regional ocean model implementation for the Mid-Atlantic Bight and Gulf of Maine (MABGOM, thereafter). The structure of this paper is as follows: Section 2 provides a description of MABGOM model setup including a brief overview of the theory underpinning the ROMS I4D-Var system. The performance of the data assimilative modeling system is described in section 3. Section 4 discusses the evolution of the Warm Core Ring, detailed shelf/slope exchange processes introduced by the WCR, and vorticity diagnostics. Discussions and a summary are given in section 5.

2. Model and Configuration

2.1. Forward Model

The Regional Ocean Modeling System (ROMS) is a free-surface, hydrostatic, primitive equation model in widespread use for estuarine, coastal, and basin-scale ocean applications (www.myroms.org/papers). ROMS employs split-explicit separation of fast barotropic and slow baroclinic modes, and is formulated in vertically stretched terrain following coordinates using algorithms described in detail by *Shchepetkin and McWilliams* [2005] and *Haidvogel et al*.[2008]. A redefinition of the barotropic pressure-gradient term is also applied in ROMS to reduce the pressure-gradient truncation error. Our MABGOM model domain is bounded by Cape Hatteras in the southwest and Nova Scotia in the northeast (Figure 1). The model's horizontal resolution is 10 km in the along-shelf direction, and 5 km in the cross-shelf direction. Vertically, there are 36 terrain-following levels in the water column with higher resolution near the surface and bottom in order to better resolve ocean boundary layers. We applied the method of *Mellor and Yamada* [1982] to compute vertical turbulent mixing, as well as the quadratic drag formulation for the bottom friction specification.

Open boundary conditions were defined by using 1/12° daily HYCOM (Hybrid Coordinate Ocean Model) NCODA (Naval Research Laboratory Coupled Ocean Data Assimilation) output [*Chassignet et al*., 2006]. The *Flather* [1976] condition was used for boundary sea level and transport specifications. Because the current implementations of the ROMS tangent-linear and adjoint models do not allow for radiation boundary conditions, the clamped boundary conditions were used for the 3-dimensional boundary temperature, salinity and velocity. We employed a 5-grid-point sponge layer (with 5 time higher viscosity) near all three open boundaries to alleviate any wave reflections produced by the clamped conditions. Within the sponge layers, the climatological tracer nudging was also applied to relax temperature and salinity fields back to HYCOM solutions over a timescale of 1 day.

The HYCOM/NCODA data set has a systematic salinity bias on the shelf. As such, the data were corrected against the HydroBase [*Curry*, 2001] temperature and salinity climatology first before serving as initial conditions, boundary conditions as well as climatology. Specifically, the annual means of temperature and salinity

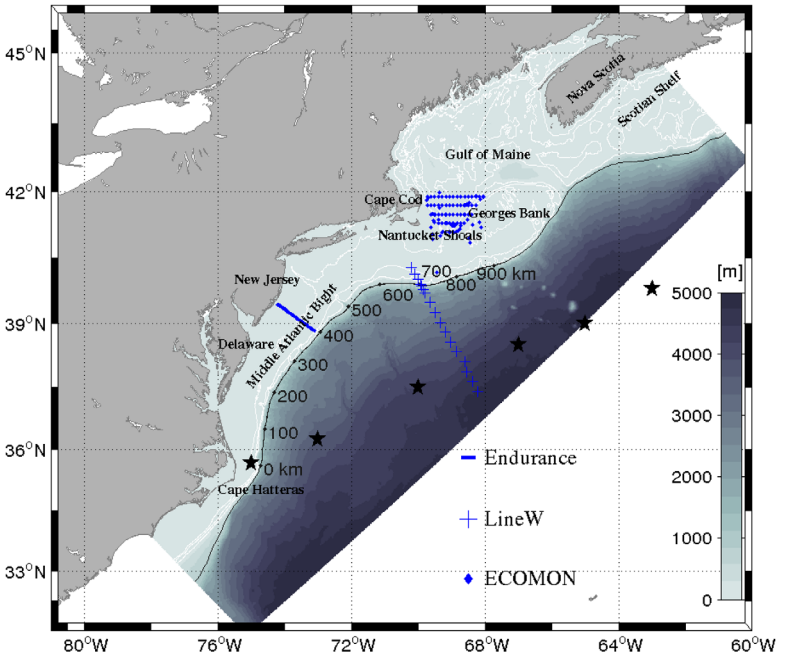

Figure 1. Mid-Atlantic Bight and Gulf of Maine model domain. The bathymetry is shown in color. The Endurance line along which gliders transects were taken is denoted in thick blue line. Line-W R/V Oceanus CTD stations are shown in blue crosses. ECOMON CTD stations in May 2006 are shown in blue diamonds. The 50, 100, and 200 m isobaths are shown in white contours. Also shown are the 1000 m isobath (smoothed) and the relative along-isobath distance with respect to the starting point. Black stars represent the mean Gulf Stream path determined by the 15°C isotherm at 200 m [*Joyce et al.*, 2000].

from the NCODA data set were replaced by annual means from the HydroBase while the daily variations were retained. Similarly, the mean dynamic height (DH) and associated geostrophic transport (GT) were computed based on the HydroBase annual mean temperature and salinity. The resulting annual mean DH and GT at the boundaries were used to correct their corresponding mean values in NCODA.

Three hourly and 35 km resolution surface forcing data were obtained from the National Center for Environment Prediction (NCEP), North America Regional Reanalysis (NARR). Air-Sea fluxes of momentum and buoyancy were computed from the standard bulk flux formulas [*Fairall et al.*, 2003] using the NARR archive including surface winds, air temperature, air pressure, relative humidity, short wave radiation, long wave radiation, cloud coverage, and precipitation. Surface net heat flux was further corrected using the 10 km resolution NOAA CoastWatch blended SST with a relaxation time scale of 0.5 day [*Chen and He*, 2010]. Fresh water runoff from nine major rivers in the region was also considered. These include the St Johns, Penobscot, Kennebec, Androscoggin, Merrimack, Connecticut, Hudson, Delaware, and Potomac Rivers. For each of them, United State Geological Survey (USGS) real-time river runoff measurements were used to specify freshwater volume transport.

The data assimilation experiment focused on a 2 month period from 1 April to 30 May 2006, but the non-data assimilative forward model simulation was integrated for 4 years from 1 January 2004 to 31 December 2007. MABGOM forward solutions were compared against extensive observations including coastal sea levels, satellite altimeter sea surface height, mooring and glider observed hydrography, and long-term mean shelf current times series. The low-frequency circulation variability were all reasonably captured, as demonstrated by the mean sea surface height (SSH) comparison in April–May 2006 (Figure 2). The model well resolved the Gulf Stream, the relative low SSH in the Slope Sea and relative high SSH along the coast which is related to the river runoff. The exact location of the Warm Core Ring/eddy was not simulated well compared to satellite observations. In particular, the mean eddy location in the forward model solution was located more to the southwest and closer to the Gulf Stream. Our goal was to apply data assimilation to improve the low frequency hydrodynamic simulation during this period to achieve better understanding of the dynamical processes associated with the MAB shelf circulation and the WCR. As such, tides were neglected in this study.

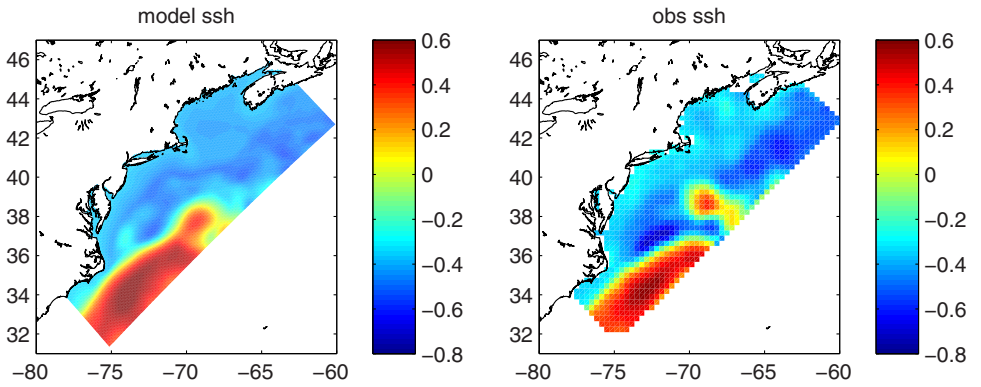

Figure 2. Comparison of 2 month mean (April–May 2006) sea surface height (SSH) from the forward model simulation (MABGOM) and AVISO satellite observed SSH (constructed by adding model simulated mean (2004–2007) sea level to the original sea level anomaly).

2.2. 4-D Variational Data Assimilation

2.2.1. ROMS I4D-Var

The ROMS 4-Dimensional Variational (4D-Var) Data Assimilation (DA) system includes the nonlinear forward model (NLROMS), the tangent linear model (TLROMS) and its adjoint (ADROMS). The system provides powerful toolsets for conducting various types of model prediction and analysis on complex ocean circulations [e.g., *Moore et al*., 2004, 2011b; *Di Lorenzo et al*., 2007; *Powell et al*., 2008, 2009; *Wilkin et al*., 2008; *Broquet et al*., 2009, 2011; *Zhang et al*., 2010; *Matthews et al*., 2012]. Among which, the ROMS I4D-Var method applies the incremental formulation described by *Courtier et al*. [1994]. This method is based on the assumption that the increments are small compared to the background fields, in which case increments are approximately described by a first-order Taylor expansion of NLROMS and can be integrated forward in time by TLROMS and backward in time by ADROMS. A brief overview of the incremental method and important concepts are given below to aid discussions in later sections. More details on its implementation in ROMS can be found in *Powell et al*. [2008] and *Moore et al*. [2011a].

Let us denote the model state vector as $\boldsymbol{x}$, composed of the prognostic variables: the sea surface height ζ at all model grid horizontal locations, and the potential temperature T, salinity S, and the velocities (u, v), at all model grid 3-D locations, such that $\boldsymbol{x} = (\zeta, T, S, u, v)^T$, where superscript T denotes the vector transpose. We represent the NLROMS symbolically as $(\partial \boldsymbol{x}/\partial t) = M(\boldsymbol{x})$, where M denotes the model operators. The goal of 4D-Var is to identify the best estimate circulation, also referred as the analysis or posterior, namely $\boldsymbol{x}^a(t)$. The solution $\boldsymbol{x}(t_i)$ of NLROMS will depend upon the choice of initial conditions $\boldsymbol{x}(t_0)$, boundary conditions $\boldsymbol{b}(t)$, and surface forcing $\boldsymbol{f}(t)$, all of which are subject to uncertainties. In 4D-Var, $\boldsymbol{x}(t_0)$, $\boldsymbol{b}(t)$, and $\boldsymbol{f}(t)$ are referred as control variables and define the control vector $\mathbf{z}$, where $\mathbf{z}=\left(\mathbf{x}(t_0)^T, \mathbf{b}(t)^T, \mathbf{f}(t)^T\right)^T$. The 4D-Var problem is then reduced to identifying the appropriate combination of control variables that yield the best estimate $\boldsymbol{x}^a(t)$ over a chosen time interval.

The estimate $\boldsymbol{x}^a(t)$ is identified by minimizing a nonlinear cost function J_{NL}, which is a measure of the squared difference between observations and the solution from the background NLROMS simulation, such that $J_{NL}=\frac{1}{2}(\mathbf{z}-\mathbf{z}_b)^T\mathbf{B}^{-1}(\mathbf{z}-\mathbf{z}_b)+\frac{1}{2}(\mathbf{y}-H(\mathbf{x}))^T\mathbf{R}^{-1}(\mathbf{y}-H(\mathbf{x}))$, where H is the nonlinear observation operator that maps the state vector to the observation points and $\mathbf{y}$ is the vector of observations. $\mathbf{B}$ and $\mathbf{R}$ are model background covariance and observation error covariance matrix, respectively, and their specifications will be discussed later. The incremental formulation of 4D-Var [*Courtier et al*., 1994] proceeds by linearizing the problem about the background which leads to the incremental form of the cost function $J = J_b + J_o$, given by:

$$J_b=\frac{1}{2}\delta\mathbf{z}^T\mathbf{B}^{-1}\delta\mathbf{z}, \tag{1}$$

$$J_o=\frac{1}{2}(\mathbf{G}\delta\mathbf{z}-\mathbf{d})^T\mathbf{R}^{-1}(\mathbf{G}\delta\mathbf{z}-\mathbf{d}), \tag{2}$$

where $\delta\mathbf{z}=\left(\delta\mathbf{x}(t_0)^T, \delta\mathbf{b}(t)^T, \delta\mathbf{f}(t)^T\right)^T$ is the control vector of increments and matrix $\mathbf{G}$, is tangent linear model sampled at the observation points. The vector $\mathbf{d} = \mathbf{y} - \mathbf{Hx}$ is the innovation where $\mathbf{H}$ is the tangent

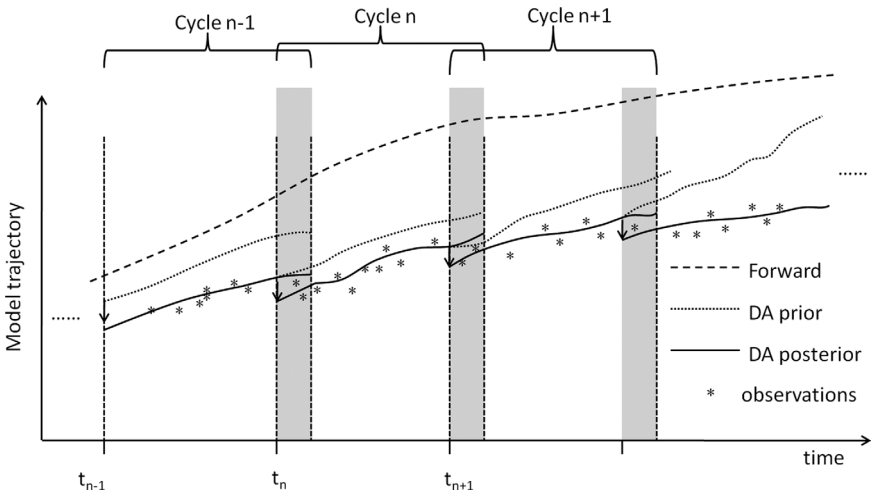

Figure 3. A schematic showing the assimilation windows and differences in forward, DA prior and DA posterior simulations. Shaded columns represent overlaps between windows. Trajectories of forward model, data assimilation (DA) prior simulation, and DA posterior simulation are denoted in dashed, dotted, and solid curves, respectively. Stars represent available observations.

linearization of the observation operator H. We seek the solution $\delta\mathbf{z}^a$, where $\delta\mathbf{z}^a$ yields the minimum value of J. $\delta\mathbf{z}^a$ is identified iteratively by solving a sequence of linear least squares minimizations (inner loops) repeated with periodic updates to the background about which **G** is linearized (outer loops). In ROMS 4D-Var, a conjugate-gradient (CG) algorithm based on *Fisher* [1998] is used to achieve the minimization. The numbers of outer loops and inner loops were fixed to yield a good estimate of the minimum of *J*. During each inner loop, TLROMS is used to propagate the increments forward in time to evaluate (2), and ADROMS yields the gradient of J, namely $\nabla J(\delta\mathbf{z})$, which is used by the CG algorithm to identify $\delta\mathbf{z}^a$ and the minimum of *J*. The best estimate $\delta\mathbf{z}^a$ is identified at the end of the iterative process. In this study, ROMS 4D-Var was allowed to adjust the initial condition, boundary conditions, and surface forcing, such that the optimal increment $\delta\mathbf{z}^a$ is applied to initial, boundary, and surface conditions after the minimization process.

Data assimilation can be performed within each of many sequential time windows that together span the entire analysis period (Figure 3), thus in each assimilation window the tangent linear approximation should be valid. At the beginning of each assimilation window, the best estimate initial condition $\mathbf{x}^a(t_0)$ derived from the previous window (or directly given for the first window) is used to compute a forecast with NLROMS. This forecast provides the background trajectory or the optimal model trajectory when observational data are not available in the current assimilation window. In this study, the DA was done with overlapped assimilation windows and we will discuss that in section 2.3.2.

2.2.2. Observational Data

Observations from various different in situ and satellite platforms were assimilated in this study.

2.2.2.1. AVISO Sea Surface Height Anomaly (SSHA)

A merged product composed of data from TOPEX/Poseidon, Jason-1, Envisat, and GFO measurements. The gridded SSHA field is available every day with horizontal resolution of 1/3°. For our application, the anomalies are converted to the sea surface height by adding the 4 year (2004–2007) mean sea level computed from MABGOM simulation. The AVISO gridded maps are based on optimal interpolations with realistic correlation functions. Comparing to along-track data (∼10%), the merged product significantly improves the estimation of mesoscale signals [*Le Traon and Dibarboure*, 1999; *Pascual et al*., 2006]. Considering the uncertainty of the satellite altimeter product in the coastal ocean, we excluded SSHA data located shoreward of the 200 m isobath from the assimilation.

2.2.2.2. Blended SST Data

The SST product developed by the NOAA CoastWatch is a blended product of SST observations from GOES, AVHRR and MODIS satellites. This product is available every day from July 2002 to present with a horizontal resolution of 10 km.

2.2.2.3. In Situ T and S Profile Data

Quality controlled hydrographic data were processed by the European Union ENSEMBLES project (EN3). These data are archived by the UK Met Office [*Ingleby and Huddleston*, 2007], providing valuable subsurface hydrographic observations. Within the MABGOM domain, EN3 contains in situ observations from a variety of instruments and platforms including expendable bathythermographs (XBT), Argo floats, and Conductivity, Temperature, Depth (CTD) profiles from the World Ocean Database (WOD) 2005, the Global Temperature Salinity Profile Program (GTSPP), and the USGODAE Argo Global Data Assembly Centers (GDAC). Other miscellaneous hydrographic data from volunteer observing ships are also included in EN3.

2.2.2.4. Endurance Line Glider T and S Data

Repeated Endurance line glider surveys have been conducted by Rutgers University on the New Jersey shelf since November 2003 (Figure 1). The Endurance Line is approximately 120 km long, generally extending from 20 m isobath to the shelfbreak. Hydrographic data are collected by Slocum Coastal Electric Gliders, which cycle from the surface to 3–5 m above the bottom while moving forward at an average speed of 24 km per day. The glider data [*Castelao et al*., 2008] used here are temporal averages of original Endurance line data. Six realizations (9, 15, 19, 22, 29 April and 20 May) of cross-shelf temperature and salinity data were assimilated.

2.2.2.5. Line-W CTD Data

Woods Hole Oceanographic Institution operates hydrographic surveys along Line-W, which is one component of a long-term climate observing system located on the continental slope south of New England (Figure 1). Line-W contains an array of moored instruments and also shipboard observations. The temperature and salinity observations used in this study came from 17 shipboard CTD casts from R/V Oceanus cruise 421 in April 2006. The cruise sampled a transect from the continental shelfbreak to the continental slope between 5 April and 15 April 2006, during which period a Warm Core Ring was located in the slope sea.

The observations were averaged to form "super observations," so that within each model grid cell and at each model time step there is no more than one observation of a given state variable. This procedure significantly reduces data redundancy, and the standard deviation of the observations that contribute to each "super observation" was used as a measure of the error of representativeness.

The observation error covariance matrix $\mathbf{R_i}$ was chosen to be diagonal parameterization so that observational errors are assumed uncorrelated in space and time [*Moore et al*., 2011b]. Observational error was assigned as a combination of the variance of the measurement error and error of representativeness. While the error of representativeness was based on the variance of the super observations, measurement error variances were chosen independently of data source, which allows various weightings for different types of data [*Broquet et al*., 2009]. We chose measurement error of 0.02 m for SSH data, which is the precision of altimetry. Measurement error for blended SST was taken to be 0.4°C [*Powell et al*., 2008]. For in situ profile data, glider hydrography data and Line-W CTD data, measurement errors of 0.1°C and 0.1 were used for temperature and salinity, respectively. In this study, either the measurement error or the error of representativeness was used as observational error in **R** depending on which is the larger of the two. The spatial distributions of super observations of SSH, SST and UK MET office T/S profiles are shown in Figure 4. SSH and SST on the first day of DA run (1 April 2006) are plotted, along with positions of all available in situ temperature and salinity profiles over the 2 month study period (1 April to 31 May). On 1 April, a large Gulf Stream meander had already formed and was located in the deep sea close to the continental slope. The sea surface height in the center of the meander was ~0.6 m higher than the surrounding waters, whereas the surface temperature of the ring was ~10°C higher than ambient slope water. The temporal distribution of super observations (Figure 4) shows that the majority of observations that go into the DA system are satellite observed SST, which had a total of 574,817 realizations. Due to the lower spatial resolution (~1/3°) and exclusion of coastal data, the total number of SSH realizations is 41,880. The in situ temperature and salinity profiles contribute 23,870 and 20,243 observations, respectively. The Endurance line glider survey provides 4932 temperature and salinity realizations, whereas the Line-W CTD casts yield a total of 966 observations. We note that while the T/S profile data are less in number, they provide vital subsurface information for data assimilation.

2.3. Data Assimilation Setup

2.3.1. Covariance Modeling

The parameterization of model background error covariance matrix **B** determines the way in which observational information is propagated to nonobservational variables. Therefore, proper definition of **B** has critical

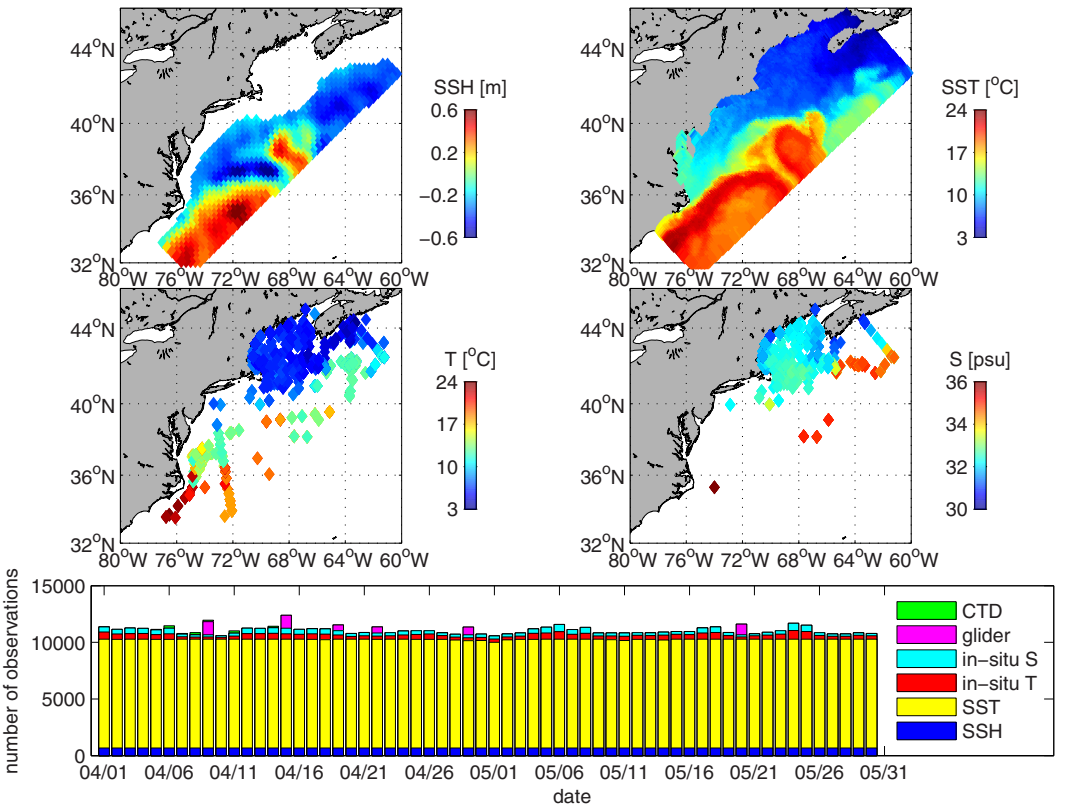

Figure 4. Super observations of sea surface height, sea surface temperature, in situ temperature profiles, and in situ salinity profiles. Only SST and SSH on 1 April 2006 are shown while all profiles collected during the assimilation period (1 April to 31 May 2006) are shown with their surface values. Temporal distributions of super observations are also shown. SSH, SST, in situ temperature profiles, in situ salinity profiles, Endurance line glider T/S observations, and Line-W CTD casts are shown in blue, yellow, red, cyan, magenta, and green, respectively.

influence on the data assimilation performance. **B** comprises the initial condition background (or prior) error covariance matrix $\mathbf{B_x}$, open boundary condition background error covariance matrix $\mathbf{B_b}$, and surface forcing background error covariance matrix $\mathbf{B_f}$. Each error covariance matrix can be modeled as $\mathbf{B}=\mathbf{K}_b \sum \mathbf{C} \sum \mathbf{K}_b^T$, where **C** is a univariate correlation matrix, $\sum$ is diagonal matrix of error standard deviations, and $\mathbf{K}_b$ is multivariate balance operator. In this study, we decided not to use the balance operator because it has its own set of technical complications. For example, the operator for the T-S relation and operator for free surface based on the level of no motion assumption are generally invalid in coastal ocean that we are dealing with in this study. The standard deviation $\sum$ is computed on a monthly basis using the MABGOM forward simulation over 2004–2007. The univariate correlation matrix is further factorized as $C=\Lambda L_v^{1/2} L_h^{1/2} W^{-1} L_v^{T/2} L_h^{T/2} \Lambda$, where Λ is a matrix of normalization coefficients, L_v (L_h) is vertical (horizontal) correlation function, W is the diagonal matrix of grid volumes [*Moore et al*., 2011a]. The correlation matrices, L_v and L_h, with their associated normalization factors Λ, are computed as solutions of diffusion equations following *Derber and Rosati* [1989] and *Weaver and Courtier* [2001]. The length scales chosen for L_v and L_h represent the decorrelation scales from a typical increment, and are currently assumed to be homogenous and isotropic. In our setup, the decorrelation length scales used to model the B_x were 50 km in the horizontal and 30 m in the vertical for all state variables. The correlation lengths of state variables for B_b were chosen to be 100 km in the horizontal and 30 m in the vertical. The horizontal correlation scales for B_f were set as 100 km for background surface tracer and momentum fluxes. Those values are comparable with *Moore et al*. [2011b] and are reasonable since the focus here is the WCR.

2.3.2. Assimilation Window

To reproduce the WCR event in spring 2006, we chose to run ROMS I4D-Var from 1 April to 31 May 2006, covering the entire life span of the ring, including different phases of (i) the Gulf Stream meander development, (ii) detachment of the meander, (iii) formation of the ring, (iv) interaction of the WCR and the shelf-break, and (v) retreat and reattachment with the Gulf Stream. An assimilation window of 3 day was chosen

because the Gulf Stream and WCR that we were targeting here are very nonlinear (with relative vorticity being $> f$). A short assimilation window will preserve the tangent linear approximation and effective control of model trajectories [*Wilkin et al*., 2008; *Powell et al*., 2008; *Broquet et al*., 2009]. We performed sensitivity experiments using longer assimilation windows, and confirmed that the 3 day window was a good choice to both effectively reduce the model-data misfits and achieve smooth model trajectories at the same time. Additionally, we also chose a 1 day overlap between assimilation windows (Figure 3), so 3 days of observations were utilized during each window and the circulation at the end of the 2nd day serves as the initial guess for the next assimilation window. Through such overlapping, 2/3 of the observational data set was used twice, but in different assimilation windows, and no account is taken here of the correlation between the background error and observation error during day 3 of each cycle. This allowed us to utilize full 3 day data to provide a good constraint to model trajectories and start the next priors at the beginning of the 3th day for better initial conditions [*Powell et al*., 2009]. During the assimilation period, a total of 30 windows of assimilation were performed individually and the posterior information can be carried over from one window to the next.

Choosing the numbers of inner and outer loops is a trade-off among computational cost, the level of convergence of the CG algorithm, and the need to update the cost function shape. Our sensitivity experiments revealed that using several outer loops had a weak influence on the cost function convergence, in that for a given total number of loops (i.e., the product of the numbers of inner loops and outer loops), the final cost function was similar regardless of the combination of inner and outer loops. In our case, we therefore chose 2 outer loops and 8 inner loops for each assimilation window. So the nonlinearity was updated one time during each assimilation windows to account for the nonlinear processes related to the WCR. We found that a total number of 16 loops were sufficient to yield a reasonable estimate of the minimum of *J*, in the sense that the rate of change in *J* indicated by the differences between its final value and the optimal solution is small ($<$1%) compared with the difference between the initial and final values of *J*.

3. Data Assimilative Model Performance

In this section, we demonstrate the performance of the data assimilative model, specifically subsurface hydrographic bias reduction and independent data comparisons. More details on the cost function reduction and surface error correction are given in *Chen* [2011].

3.1. Reductions of Model Error

The model-observation error bias $\frac{1}{N}\sum_{i=1}^{N}\left(y_i^m - y_i^o\right)$ was computed, where N is the number of observations, and y_i^m and y_i^o are simulated and observed state variables, respectively. The error bias reflects the average discrepancy between model and observation. It is one component of Root-Mean-Square Error, RMSE [*Taylor*, 2001], in that $(\text{RMSE})^2 = (\text{Error Bias})^2 + (\text{Error STD})^2$. Here RMSE is $\frac{1}{N}\sum_{i=1}^{N}\left(y_i^m - y_i^o\right)^2$, and error STD is defined as $\left(\frac{1}{N}\sum_{i=1}^{N}\left(y_i^m - \overline{y_i^m} - (y_i^o - \overline{y_i^o})\right)^2\right)^{\frac{1}{2}}$, where $\overline{y_i^m} = \frac{1}{N}\sum_{i=1}^{N}\left(y_i^m\right)$ and $\overline{y_i^o} = \frac{1}{N}\sum_{i=1}^{N}\left(y_i^o\right)$. Different from RMSE, the error bias provides more specific information on whether the model systematically overestimates or underestimates observations.

Biases between the model simulation and observed temperature and salinity, including T/S profiles from UK MET office, glider T/S along Endurance line and shipboard CTD observations from Line-W archive were computed to evaluate the model subsurface performance. Since most of the temperature and salinity data are located on the continental shelf (Figure 4), we focused on the DA performance in the coastal region. The vertical profile of temporal (2 month) bias is shown in Figure 5 (top). Near the sea surface, temperature from the forward model has a bias of 1.5°C, suggesting the model overestimates temperature in the upper water column. Temperature bias decreases at depth, but becomes negative around $\sim$ 40 m. At 150 m, the temperature bias exceeds -2°C. Such a vertical distribution shows that the forward model overestimates (underestimate) ocean temperature shallower (deeper) than 40 m. Data assimilation significantly reduces the bias. The temperature bias in the DA prior simulation is $\sim$1°C, which is further reduced (to $\sim$0.5°C) in the DA posterior simulation.

Similar improvements are seen in salinity. The forward simulation overestimates the upper water column salinity by 0.25 and underestimates the subsurface salinity by 0.5. After data assimilation, the upper water

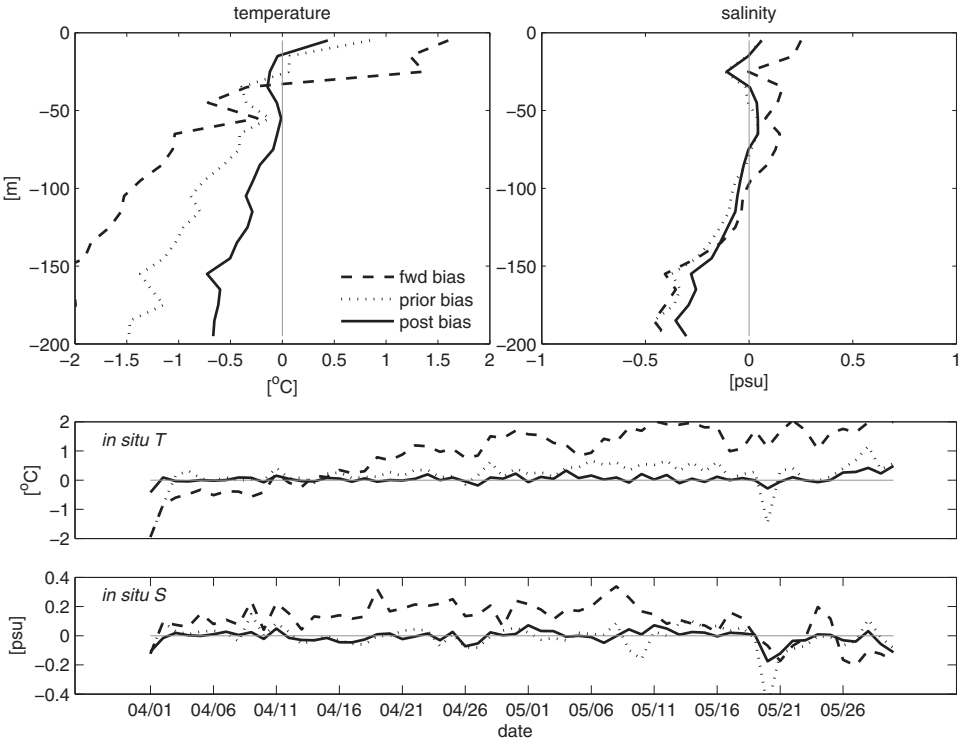

Figure 5. Subsurface tempeature and salinity Bias in forward, DA prior and DA posterior simulations. Vertical distribution of biases of temperature and salinity over the assimilation period are shown in the top two plots, with biases from the forward model, 4D-Var prior and posterior denoted shown in dashed, dotted, and solid curves. Time series of temperature and salinity biases for each simulation are also shown in the bottom plots.

column salinity bias is reduced to ∼0.1 and the subsurface bias is reduced to <0.4. We note the bias reduction in salinity is not as dramatic as in temperature because the amount of salinity data is less than that of temperature for assimilation.

Time series of the total average bias (Figure 5, bottom) provides another view of the performance of data assimilation. The temperature bias in the forward simulation ranges from −2°C at the beginning of the study period to 2°C at the end of study period. Such drifting in temperature fields is effectively removed after data assimilation. Both the DA prior and posterior simulations show that the temperature bias is reduced to a much small range between −0.5 and 0.5°C. Similar improvement is evident for salinity. After data assimilation, the salinity bias is reduced to almost to zero over the entire assimilation period, as opposed to 0.2–0.3 in the forward simulation. Overall, these comparisons indicate that I4D-Var is effective in reducing the misfit between model and observations. Although most of data being assimilated are satellite observation (SST and SSH), the results show they also help to improve the model's fidelity in resolving the subsurface hydrographic structures.

3.2. Independent Data Comparison

A more rigorous evaluation of the data assimilative simulation can be achieved by comparing model fields with nonassimilated observations. The nonassimilated data in this case are temperature and salinity profiles measured by National Oceanic and Atmospheric Administration (NOAA) Northeast Fisheries Science Center (NEFSC) Ecosystem Monitoring (ECOMON) program. ECOMON focuses on the shelf-wide ecosystem monitoring, conducting hydrography and plankton surveys 6–7 times per year over the continental shelf between Cape Hatteras, North Carolina and Cape Sable, Nova Scotia. The data we used in this study are CTD observations from 3 April to 25 May 2006. Most of the casts are located in the Massachusetts coastal waters and near the Great South Channel (Figure 1). In total, 275 temperature and salinity profiles are available for comparisons. We sorted these temperature and salinity profiles in the time ascending order with profile 1 being data taken on 3 April, and profile 275 being data taken on 25 May 2006, respectively. The

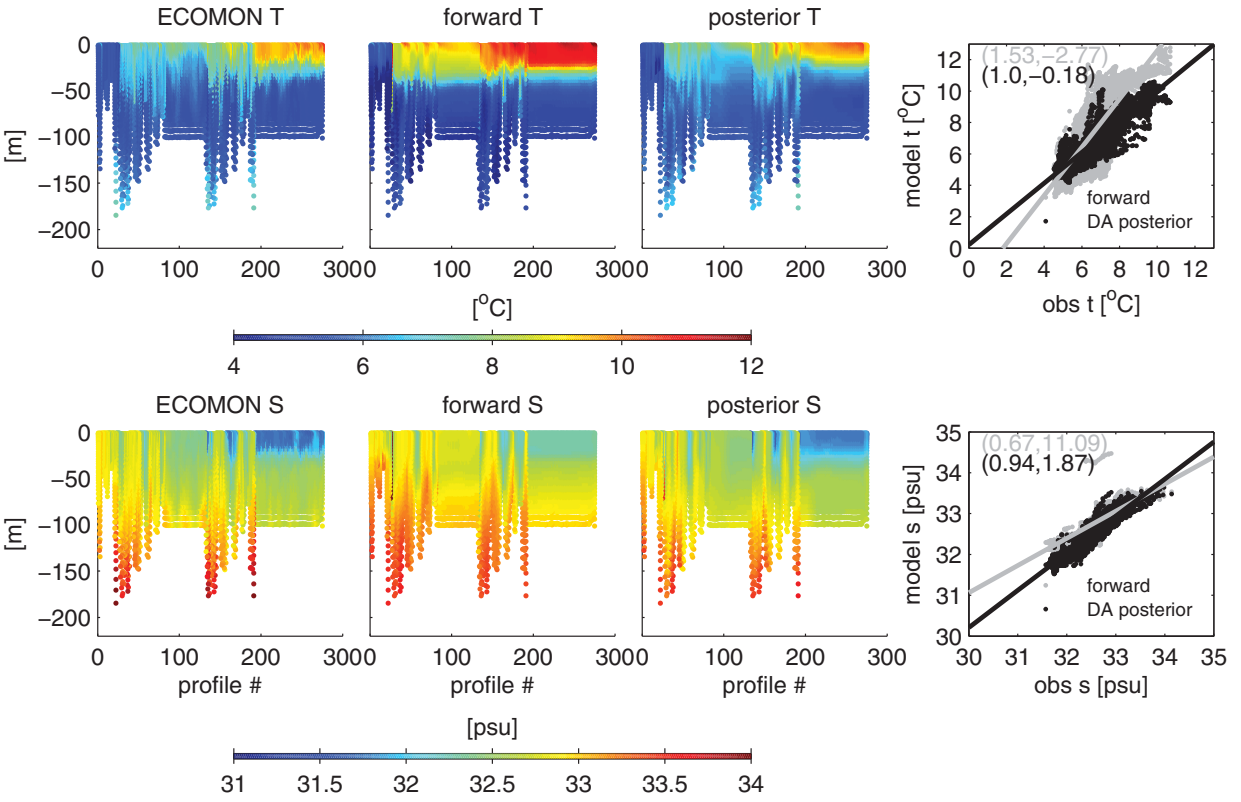

Figure 6. Comparisons of temperature and salinity between ECOMON observations, MABGOM forward model simulation, and DA posterior simulation. Point-to-point comparions of ECOMON observed versus model simulated temperature and salinity are also shown. Temperature (salinity) simulated by the forward model are shown in gray while temperature (salinity) simulated by te DA posterior simulation are shown in black. For each comparion, values of slope and intercept resulted from the linear function fitting are shown in the parentheses, respectively.

maximum depth of these CTD casts ranges from 50 to 200 m. To facilitate model comparison, we interpolated these temperature and salinity profile data onto the model vertical grid (Figure 6).

Temperature data show a clear seasonal warming trend over the 2 month period. The water column is nearly well mixed (being 4°C) in the first few profiles. The stratification starts to develop quickly afterward and by May, the surface temperature increases to ∼10°C. The forward model simulation tends to overestimate surface temperature and underestimate the subsurface temperature, producing a more stratified thermal structure. After data assimilation, we see the seasonal evolution is much better resolved and both the timing and magnitude compare favorably with in situ temperature data. The total temperature RMSE between forward simulation and ECOMON data is 1.5°C. In comparison, the total RMSE of temperature between DA posterior simulation and observation is reduced to 0.6°C, which is a ∼60% error reduction. For salinity, ECOMON data indicate a seasonal freshening trend in the upper water column, which is presumably related to increased coastal freshwater runoff in the Gulf of Maine as the season progresses. The forward model simulation is able to capture this salinity feature but the magnitude is off by nearly 1 unit. After data assimilation, the refined circulation and fresh water flux contribute to the improvement of upper water column salinity field. The total salinity RMSE is reduced from 0.30 to 0.13, which is a 57% error reduction.

A more direct point-by-point comparison provides another way to highlight data assimilative model skill in reproducing nonassimilated temperature and salinity data (Figure 6). Compared to the forward model simulation, the DA posterior simulation provides better agreement for both temperature and salinity. For temperature (salinity), the slope and intercept based on the linear fitting between observation and forward model simulation are 1.53 (0.67) and −2.77 (11.09), respectively. For DA posterior simulation, they are 1.0 (0.94) and −0.18 (1.87), respectively. Such comparisons against nonassimilated hydrographic data indicate the data assimilative model simulation significantly improves its prediction skill in both observational and

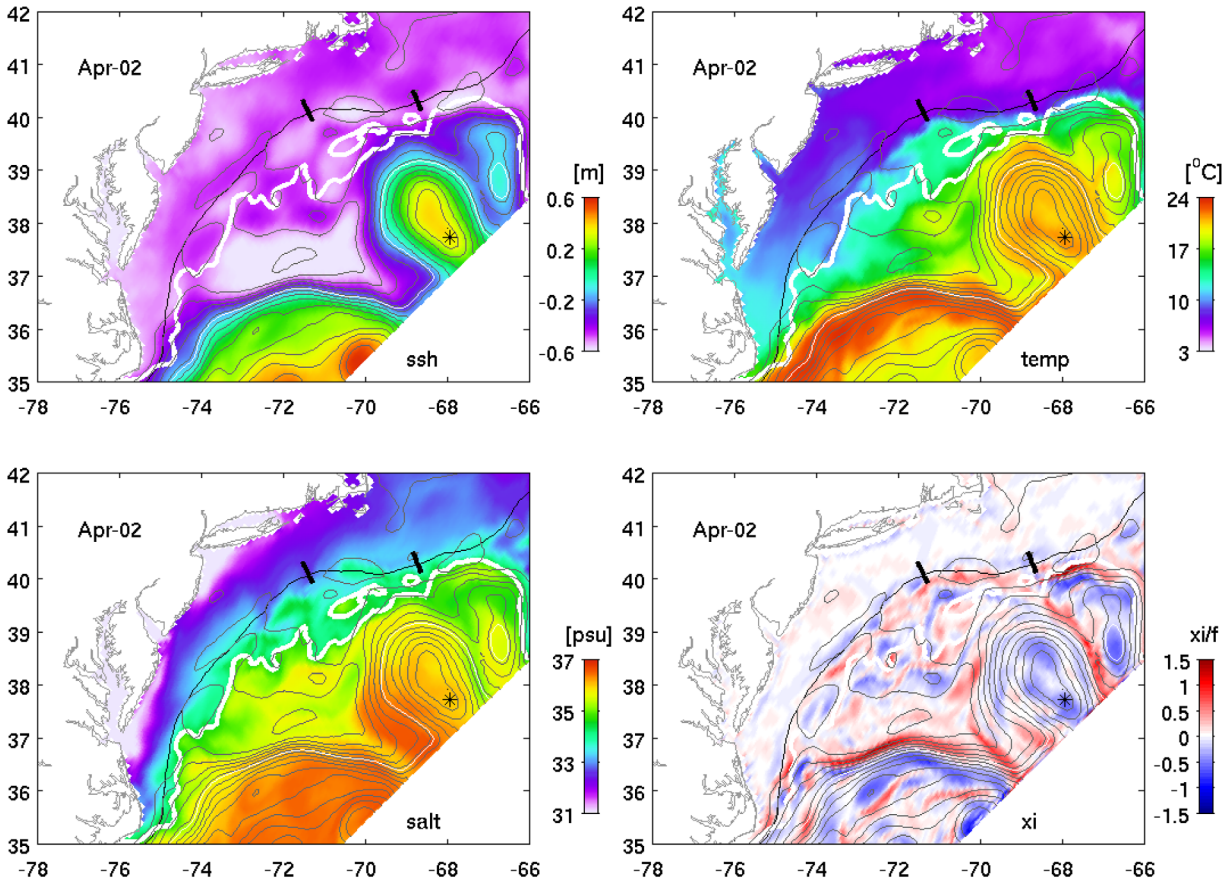

Figure 7. Surface height, surface temperature, surface salinity, and surface vorticity on 2 April 2006 from DA posterior simulation. Also shown are stream function contours (gray) and *e*-folding value (thin white contour) of maximum stream function. The center of the meander/ring is shown by the black star while its track is shown every 3 days with a black dot. The thick white curve is the 34.5 isohaline and the thin black curve is the 200 m isobath. Two cross-shelf transects are depicted by the black line segment.

model spaces, providing us the confidence of using its time and space continuous solutions to carry out further dynamical analysis.

4. Results

4.1. Evolution of the Warm Core Ring in 2006

The Warm Core Ring in this study is one of the most energetic eddies found in our study area in recent decades. Satellite imagery shows this large WCR was the result of a large Gulf Stream meander. Our data assimilative model hindcast solutions show that on 2 April 2006, a large Gulf Stream meander formed and the crest of the meander extended further northward into the slope region (Figure 7). The meander contained a large sea surface height anomaly (about 0.6 m higher than surrounding slope waters), and warm and saline waters which began to alter the hydrographic conditions of the slope sea. Negative vorticity was clearly identified near the center of the meander. At this time, the surface outcrop of the shelfbreak front in the MAB [*Linder and Gawarkiewicz*, 1998; *Bisagni et al.*, 2009] was close to the shelfbreak and oriented parallel to the local isobaths, suggesting that the direct impact of the meander had not yet reached the shelf region.

The meander continued growing in amplitude, and finally pinched off from the Gulf Stream in late April. On 22 April, the meander became a large detached WCR (Figure 8). The center of the WCR was located at 69°W, 38.8°N while the outer edge of the WCR ranged from 71°W to 67.5°W and 37.8°N to 39.8°N. At this initial stage, the temperature and salinity near the center of the WCR were about 20°C and 36, respectively. The radius of the WCR was 96–120 km based on an estimate of the *e*-folding scale of the WCR's stream function, and the depth of the WCR was up to 1000 m based on an estimate of the *e*-folding scale of the

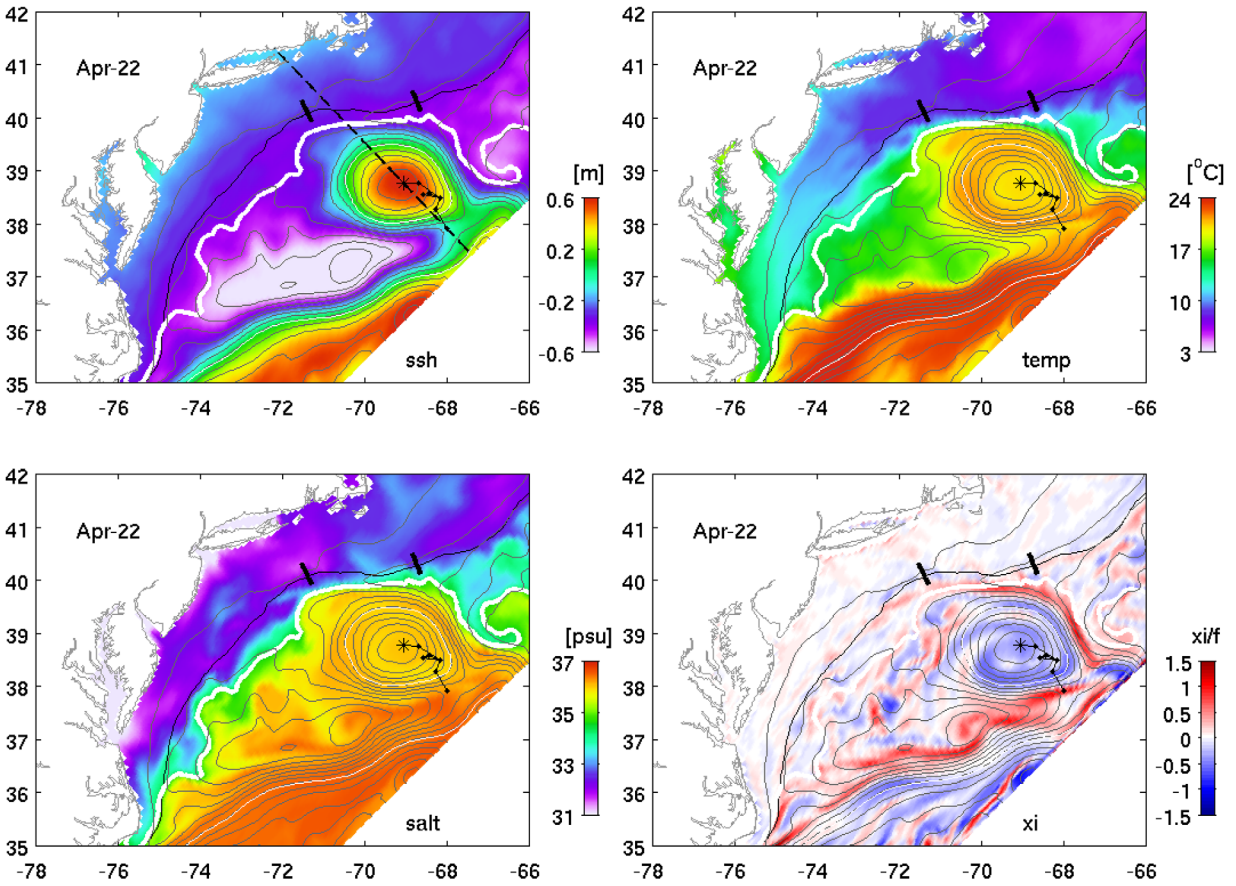

Figure 8. Same as Figure 7 but on 22 April 2006. The location of a transect through the WCR center is shown by the black dashed line.

subsurface temperature field (Figure 9). The WCR extended completely across the continental slope region with an average azimuthal velocity up to 1.5 m s^{-1}. Warm/Saline WCR waters were advected toward the shelf on the western periphery while on the eastern periphery of the WCR, offshore transport of cold/fresh shelf water (i.e., the "streamer") [*Garfield and Evans*, 1987] was observed. The sea level anomaly and intensity of negative vorticity at the center of the ring both increased compared to the early phase of the meander.

By 2 May, the detached WCR moved further toward the northwest and began to move into close proximity to the shelfbreak (Figure 10). The center of the WCR was located at 69.5°W, 38.9°N, and the northern edge of the WCR reached onshore as far as the 80 m isobath (about 40.3°N). The size of the WCR decreased to a radius of 65–87 km, and the WCR significantly impacted the shelfbreak circulation. On the western side of the WCR, the leading edge of the warm/saline WCR waters intersected the shelfbreak as shown by the outcrop of the 34.5 isohaline crossing onto the shelf. A significant portion of WCR waters intruded on the shelf, becoming entrained into the shelfbreak jet and flowed southwest along the shelfbreak. At the trailing (eastern) edge of the WCR, the streamer was directed offshore. The entrained cold/fresh shelf water moved along the eastern periphery of the WCR and reached as far as the Gulf Stream northern boundary (about 200 km south of the 200 m isobath). The large velocity shear and interaction between the WCR and shelfbreak circulation also excited westward propagating frontal waves, similar to the situation described in *Ramp et al.* [1983], introducing strong across-front flow.

On 9 May, the WCR retreated slightly to the southwest from the shelfbreak (Figure 11). The center of the WCR was at 69.3°W, 38.8°N. Without direct contact with either the topography near the shelfbreak or the Gulf Stream, the WCR shape became more circular, with a mean radius of 63 km. The warm/saline water mass entrained into the shelfbreak jet extended along the shelfbreak from south of New England to a

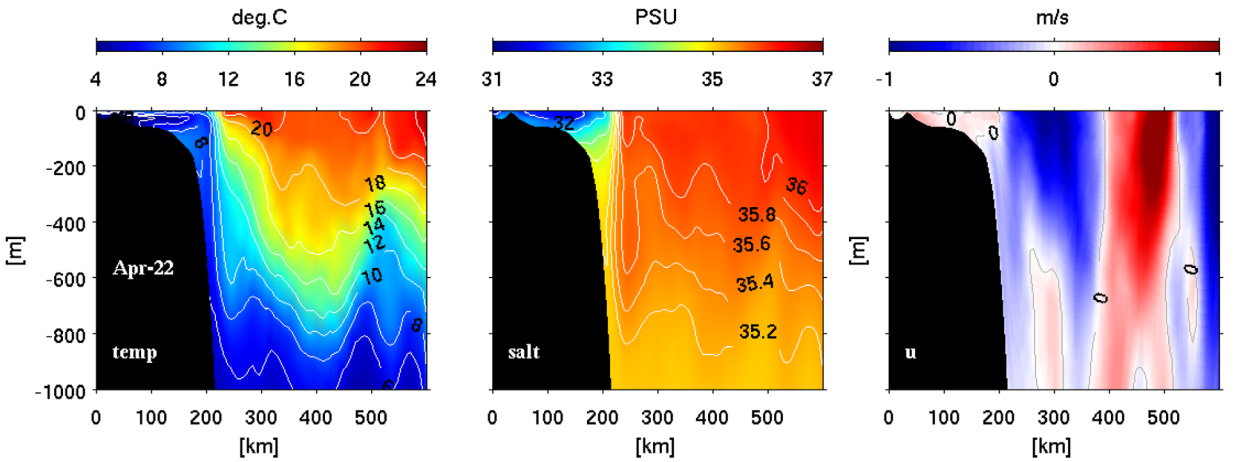

Figure 9. Cross-sectional view of temperature, salinity, and along slope velocity along a cross-shelf transect (see Figure 8) through the center of the WCR on 22 April 2006. In the third plot, the positive direction is equatorward.

position off the coast of Delaware, an alongshelf distance of 400 km. The entrainment of the WCR water mass significantly changed the shelf and shelfbreak hydrographic conditions. Further examination of the subsurface temperature and salinity fields near the shelfbreak (not shown) indicates this warm/saline water mass was about 50 m deep and its most onshore penetration was found near the 80 m isobath. This is the mean climatological position of the foot of the shelfbreak front off New Jersey [*Linder and Gawarkiewicz*, 1998]. With a mean temperature and salinity of 20°C and 34.2, respectively, this entrained water mass

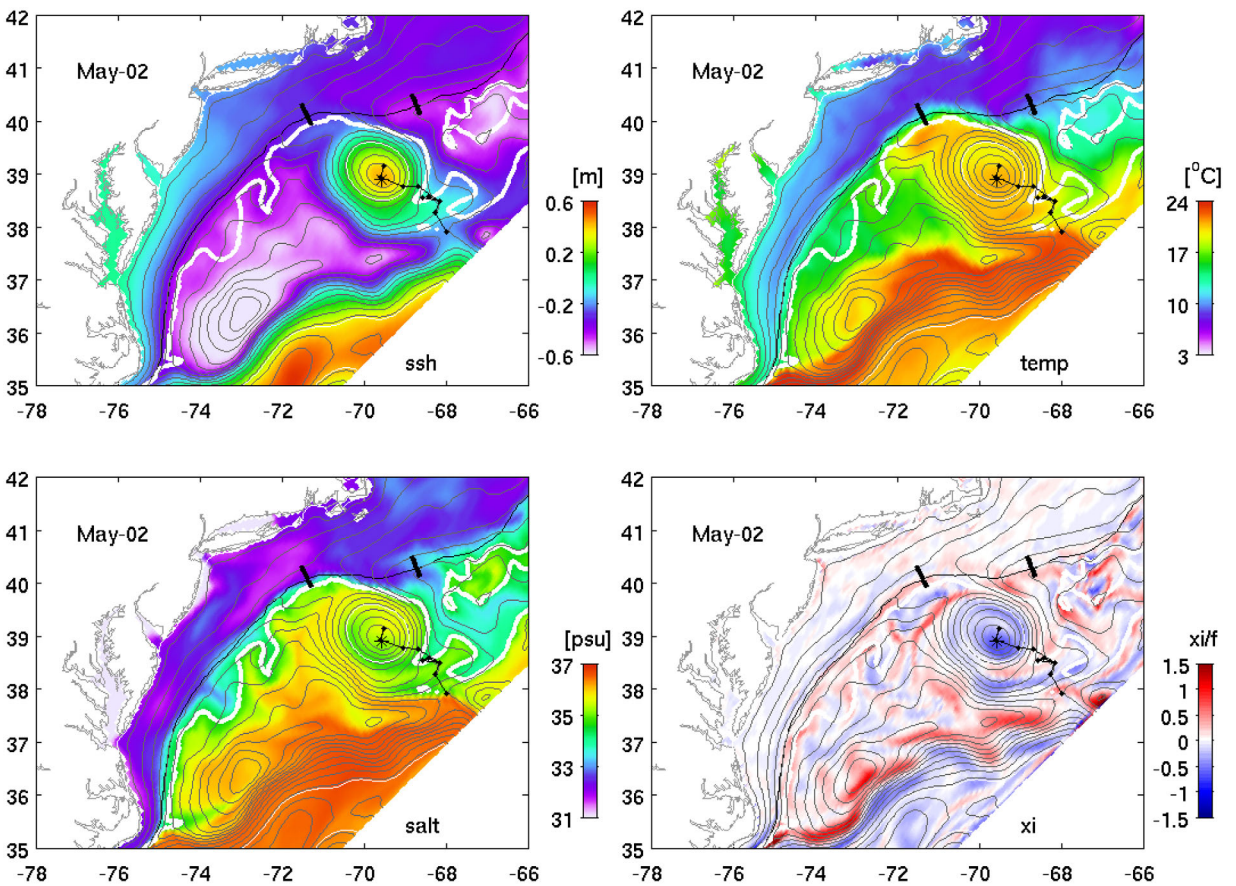

Figure 10. Same as Figure 7 but on 2 May 2006.

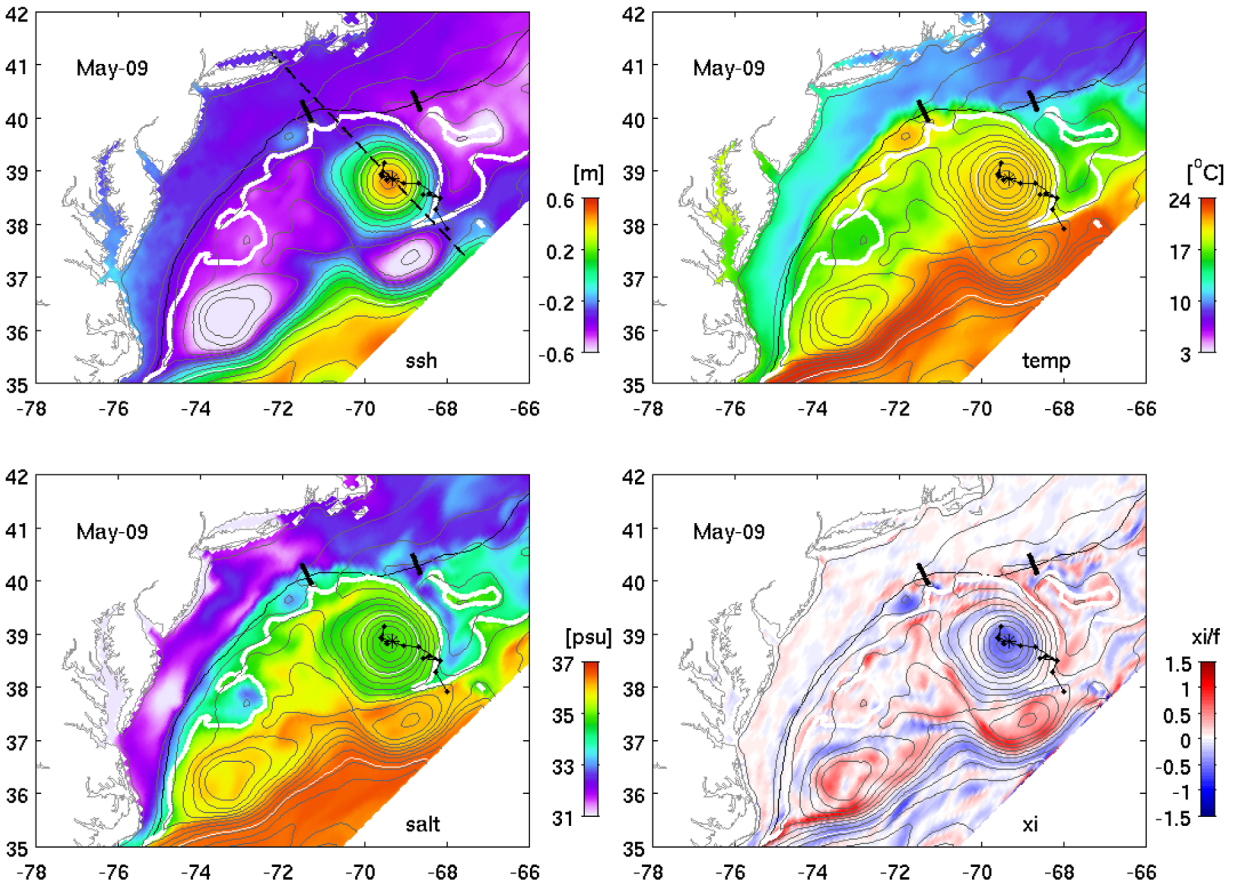

Figure 11. Same as Figure 7 but on 9 May 2006. The location of a transect through the WCR center is shown by the black-dashed line. The frontal wave feature is depicted by the curvature of the 34.5 isohaline (thick white curve).

moved to the southwest at a speed of 0.6 m s^{-1}. During this phase of WCR interaction with the shelfbreak front, the frontal wave along the shelfbreak to the western side of the WCR became more pronounced. The wavelength is estimated to be around 120 km, which is much larger than the wavelength of 23 km for the case in *Ramp et al*. [1983]. We also note that the WCR in *Ramp et al*. [1983] is smaller than the WCR in this study. At this time, the entrained shelf water (streamer) can be clearly seen on the eastern side of the WCR. The relative vorticity field in the central WCR was more uniform (0.5 f), indicating solid body rotation. At depth (Figure 12), the 16°C isotherm rose to a depth of 200 m, compared to approximately 500 m on 22 April. The subsurface (∼100 m) water mass had a maximum salinity around 35.5 while the surface water was fresher by about 1. This is consistent with findings described in *Joyce* [1984] and *Joyce et al*. [1992] and is related to the entrainment of fresh shelf water in the upper water column. The average azimuthal velocity at this time decreased to 1.3 m s^{-1}, suggesting spin-down of the WCR.

During mid-May, the WCR continued retreating southward to the Gulf Stream and decreased in size. By the end of May (Figure 13), the WCR had reattached to the Gulf Stream. The remnant warm/saline WCR water mass along the shelfbreak had already reached Cape Hatteras and moved offshore along the Gulf Stream [*Ford et al*., 1952; *Fisher*, 1972; *Gawarkiewicz and Linder*, 2006].

4.2. Shelf/Slope Exchange

The main interactions between the WCR and the shelf/slope circulation occurred in the period from 22 April to 18 May 2006. The size and pinch-off location of the ring may be the factors that limit the duration of this interaction. Due to the WCR translation across the slope in late April and its interaction with the shelfbreak in early May, significant impacts on the slope and shelf hydrography and circulation were present in the model fields. The onshore advection of WCR water at the leading (western) edge and offshore advection of shelf water at its trailing (eastern) edge induced high levels of cross-shelf exchange. The presence of the

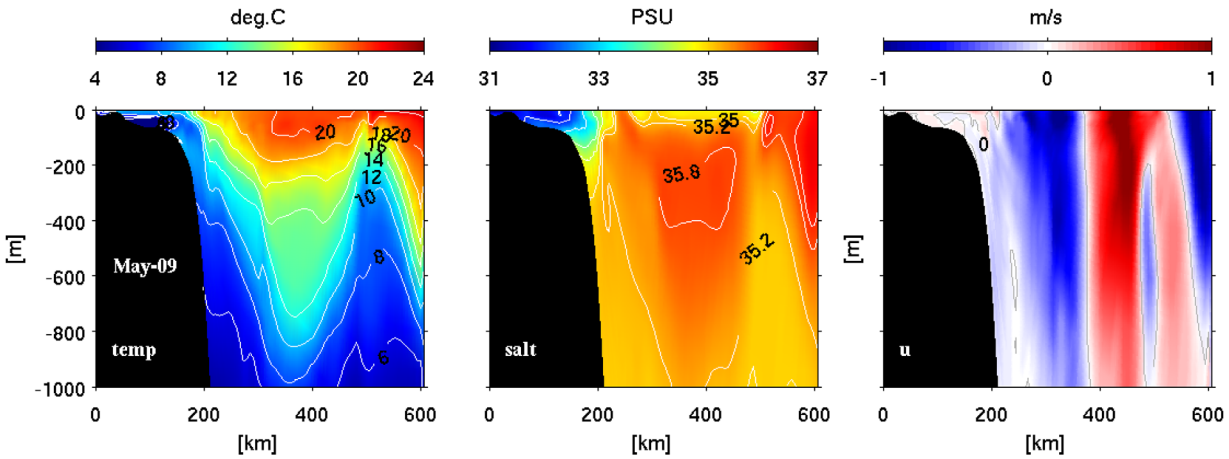

Figure 12. Same as Figure 9 but on 9 May 2006. The location of the transect is marked in Figure 11.

WCR acted as an along-shelf obstruction for the shelfbreak jet. As a result, a large streamer formed, advecting shelf water large distances offshore. In the following section, we quantify the shelf/slope exchange induced by the WCR and identify the timescale over which it occurs.

We first define a material boundary in order to calculate the exchange induced by the WCR. Considering the vertical extent of the WCR and the constraint imposed by the shelf bathymetry preventing WCR from penetrating further onto the shelf [e.g., *He and Weisberg*, 2003], we selected the 1000 m isobath for the

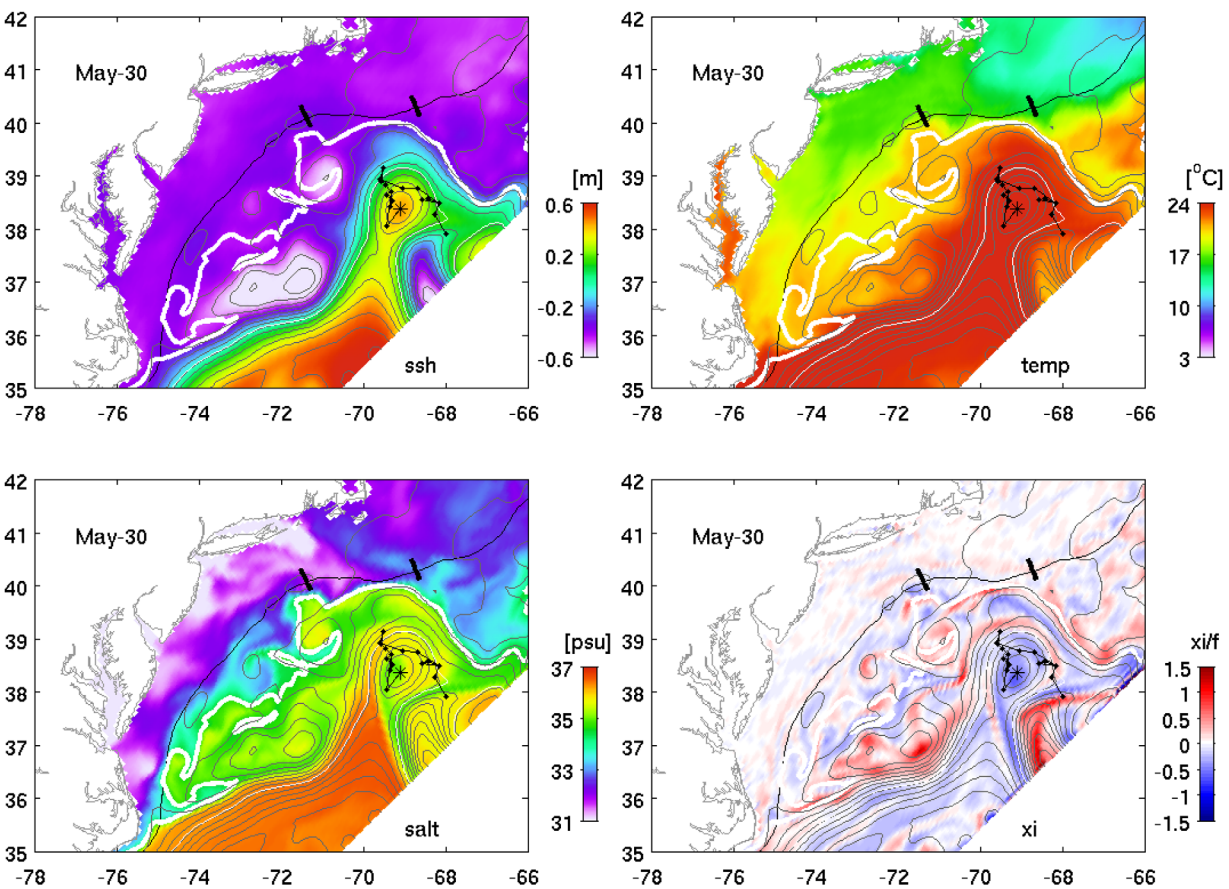

Figure 13. Same as Figure 7 but on 30 May 2006.

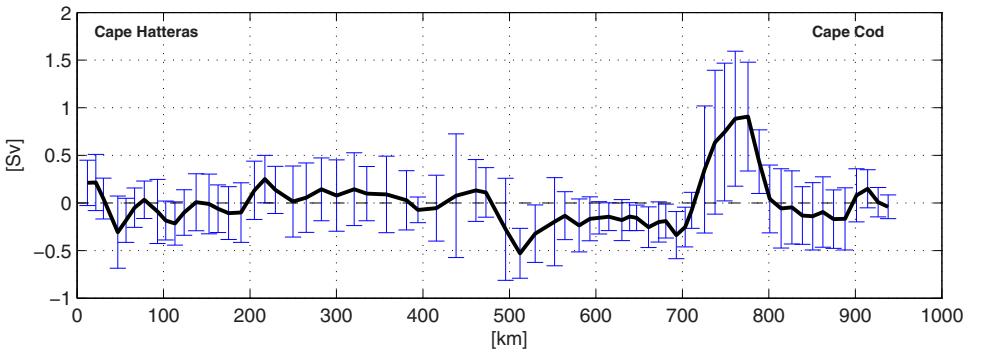

Figure 14. Cross-shelf volume transport along the 1000 m isobath (see Figure 1 for the location). Mean values (22 April to 18 May) are shown by the solid black curve while standard deviation are shown in blue. Negative values denote onshore transport while positive values denote offshore transport.

volume transport calculation. The 1000 m isobath defines a ~900 km boundary offshore of MAB from Cape Hatteras to Cape Cod (Figure 1). Posterior 3-D velocity fields were rotated into the normal and tangential components based on the local orientations of isobath. Then the normal component of velocity u_N was integrated with local depth Z and along-isobath length S to yield the volume transport values according to:

$$Q=\int_0^{s_o}\int_{-H}^{\eta} u_N(s,z)dzds. \tag{3}$$

In this analysis, we focused on the cross-shelf exchange during the time period when the WCR was near the shelfbreak, i.e., from 22 April to 18 May. The resulting spatial distribution of the cross-shelf transport was presented in Figure 14. Consistent with the findings of *Chen and He* [2010], the cross-shelf volume transport in the southern MAB was characterized by small mean values and large standard deviations. The impact of the WCR became more significant in the northern MAB (from offshore New Jersey to Nantucket Shoals, between 450 and 700 km), and the mean cross-shelf transport over this segment of the 1000 m isobath was onshore. The largest onshore transport is 0.5 Sv at this section where the leading edge of the WCR was present. The offshore transport was up to 1 Sv between ~700 and ~800 km, which was at the trailing edge of the WCR. We note the region of offshore transport was narrower than the region of onshore transport yet the transport magnitude was larger, suggesting the offshore velocity is much larger than the onshore velocity. Further examination of the modeled normal velocity fields across the 1000 m isobath (not shown) confirmed this and the maximum streamer velocity ranged from 0.2 to 0.7 m s^{-1} during the impingement of WCR.

It is important to evaluate the role of the WCR in changing the shelf water mass budget. We focus on the shelfbreak region directly impacted by the WCR (i.e., the 450–800 km portion of 1000 m isobath) to calculate total cross-shelf transport in the upper 200 m, which is typical of the maximum depth of shelf water. From 22 April to 18 May, the total cross-shelf transport was estimated to be 0.28 Sv. This is 1 order of magnitude larger than the long-term mean cross-shelf transport (0.035 Sv) estimated by *Chen and He* [2010], and similar to the mean shelfbreak jet transport (0.2–0.4 Sv) reported by *Linder and Gawarkiewicz* [1998] and *Fratantoni et al.* [2001].

The large entrainment of shelf water in the streamer can certainly change the temperature and salinity budget on the MAB shelf. The cross-shelf eddy heat and salt fluxes were estimated by calculating the integrated flux, Φ [*Garvine et al.*, 1989; *Gawarkiewicz et al.*, 2004; *Chen and He*, 2010], such that:

$$F(z)=\frac{1}{\Delta z\Delta s}\int_{z_o-\frac{\Delta z}{2}}^{z_o+\frac{\Delta z}{2}}\int_{s_1}^{s_2}\Phi(s,z')dsdz'. \tag{4}$$

For the heat flux, Φ is defined:

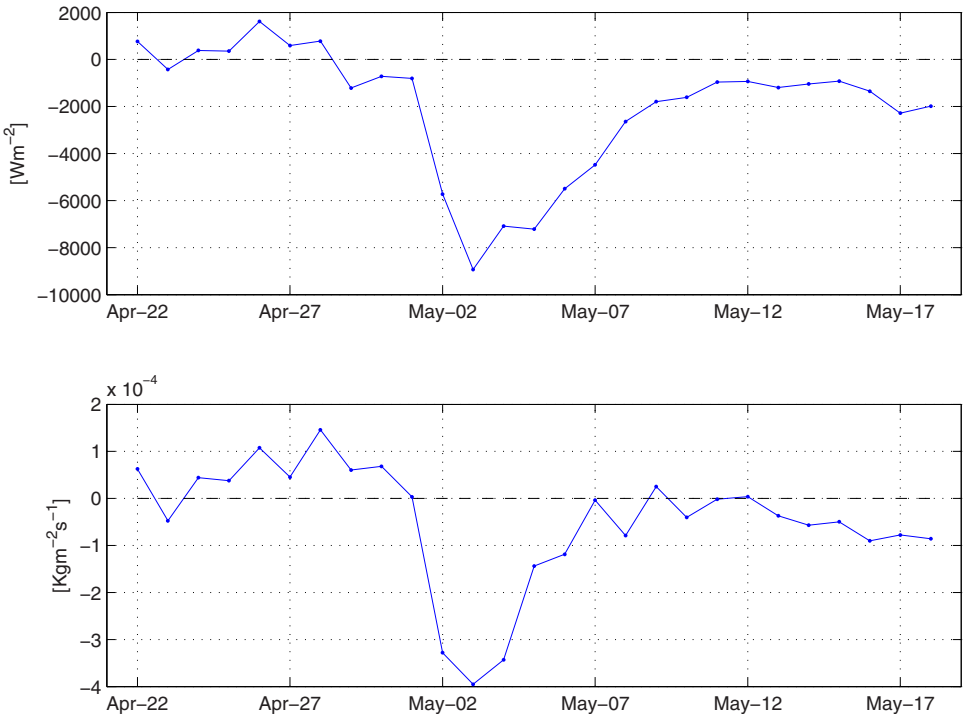

Figure 15. Cross-shelf eddy (top) heat and (bottom) salt-fluxes resulting from the WCR. Negative values represent offshore entrainment of cold/fresh shelf water.

$$\Phi = \rho C_p (T - T_m)(v - v_m). \tag{5}$$

For the salt flux, Φ is defined:

$$\Phi = \frac{\rho}{1000}(S - S_m)(v - v_m), \tag{6}$$

where S, T, and v are the salinity, temperature, and cross-shelf velocity, respectively. ρ is water density and C_p the seawater specific heat. The variables with subscript m indicate the respective mean values (based on the 2004–2007 hindcast) along the 1000 m isobath. By definition, the cross-shelf fluxes are proportional to the eddy derivation of quantities and normal velocity from their mean states. The normal velocity is defined as positive seaward, so negative F(z) means onshore heat (salt) flux which is induced by offshore transport of cold (fresh) shelf water.

Again focusing on the region where the WCR is in close proximity to the shelfbreak, the portion of the 1000 m isobath between 450 and 800 km, we calculated daily cross-shelf heat and salt fluxes during the WCR period in the upper 200 m (Figure 15). Before the WCR approached the shelfbreak, the cross-shelf heat (salt) flux was relatively small and the normal velocity fluctuated between onshore and offshore. Starting in May when the WCR was impacting the shelfbreak, large cross-shelf heat and salt fluxes were introduced. The cross-shelf heat (salt) flux peaked on 3 May with values up to ~8900 W m^{-2} (~4 × 10^{-4} kg m^{-2} s^{-1}) and remained negative throughout the first week of May 2006. In the retreating stage of the WCR, while the heat (salt) flux was still onshore (negative), the values gradually became smaller. We note that *Chen and He* [2010] estimated the long-term mean onshore heat (salt) flux to be 1000 W m^{-2} (6.7 × 10^{-5} kg m^{-2} s^{-1}) at the same region of the shelfbreak. Over a 1 week time scale for this WCR/shelf interaction event, the induced cross-shelf eddy heat (salt) increased by a factor of 6–9 compared to the long-term mean.

4.3. Vorticity Analysis

During the WCR interaction with the shelfbreak circulation and the subsequent spin-down of the ring, it is important to diagnose the vorticity evolution, and determine the processes responsible for changes in the

vorticity. This analysis focused on the first week of May 2006 when the WCR was directly interacting with shelf/shelfbreak circulation. Starting with depth-averaged momentum equation, the depth-averaged vorticity equation can be written as follows [see *Chen*, 2011] for details of derivation):

$$\frac{\partial}{\partial t} curl_z\left(\frac{\mathbf{M}}{H}\right)=\left(\frac{\partial(P_y/H)}{\partial x}-\frac{\partial(P_x/H)}{\partial y}\right)-\mathbf{M}\cdot\nabla\left(\frac{f}{H}\right)+curl_z\left(\frac{\tau_s-\tau_b}{\rho_o H}\right)+curl_z\left(\frac{\mathbf{D}}{H}\right)-curl_z\left(\frac{\mathbf{A}}{H}\right). \quad (7)$$

Here $H=h+\zeta$; $M=(\overline{u}\,\vec{i}+\overline{v}\,\vec{j})*H$; $A=A_x\vec{i}+A_y\vec{j}$; $D=D_x\vec{i}+D_y\vec{j}$, vertical integrated nonlinear advection terms are defined as:

$$A_x=\int_{-h(x,y)}^{\zeta(x,y,t)}\left(u\frac{\partial u}{\partial x}+v\frac{\partial u}{\partial y}+w\frac{\partial u}{\partial z}\right)dz,\ \ A_y=\int_{-h(x,y)}^{\zeta(x,y,t)}\left(u\frac{\partial v}{\partial x}+v\frac{\partial v}{\partial y}+w\frac{\partial v}{\partial z}\right)dz,$$

vertical integrated pressure gradient terms are defined as:

$$P_x=\int_{-h(x,y)}^{\zeta(x,y,t)}\left(-\frac{1}{\rho_0}\frac{\partial p}{\partial x}\right)dz,\ \ P_y=\int_{-h(x,y)}^{\zeta(x,y,t)}\left(-\frac{1}{\rho_0}\frac{\partial p}{\partial y}\right)dz,$$

and vertical integrated horizontal mixing terms are defined as:

$$D_x=\int_{-h(x,y)}^{\zeta(x,y,t)}D_u dz,\ D_y=\int_{-h(x,y)}^{\zeta(x,y,t)}D_v dz.$$

The term on the left-hand side of (7) is the time rate of change of depth-averaged relative vorticity. On the right-hand side, the first term, $\left(\frac{\partial(P_y/H)}{\partial x}-\frac{\partial(P_x/H)}{\partial y}\right)$ is equivalent to $J(\chi,\ 1/\mathrm{H})$, where $J(A,B)=A_xB_y-B_yA_x$, and $\chi=\frac{g}{\rho_o}\int_{-H}^{0}z\rho dz$. This term is the Joint Effect of Baroclinicity and Bottom Relief (JEBAR) [*Sarkisyan and Ivanov*, 1971; *Mertz and Wright*, 1992; *Cane et al*., 1998; *Guo et al*., 2003; *Sarkisyan*, 2006]. The second term on the right-hand side of (7) (without the minus sign) is the advection of geostrophic potential vorticity f/H (APV) [*Guo et al*., 2003]; the third and fourth terms are effects of stress and dissipation, respectively; and the last term is the nonlinear advection effect (ADV).

On 1 May, the center of the WCR, as depicted by the contours of sea surface height and negative vorticity, was located close to the shelfbreak. On 7 May, the center of the WCR retreated offshore, as shown by the negative rate of change just offshore of the shelfbreak (Figure 16c). In this period, the impinging WCR induced significant cross-shelf exchange that is particularly large for the APV term. By definition, the positive APV represents onshore transport of low PV water while negative APV stands for offshore transport of high PV water. The positive APV near the leading edge (western side) of the WCR corresponds with the onshore movement of WCR water, while the large negative APV on the trailing edge (eastern side) of the WCR corresponds to the offshore movement. The APV and JEBAR are the two largest terms in the depth-averaged relative vorticity budget. They largely balance each other, indicting the combination of baroclinicity and sloping bottom topography can generate depth-averaged transport across planetary vorticity contours. The residual of JEBAR and APV (i.e., JEBAR-APV) contributed to the increase of vorticity around the periphery of the ring as the WCR moved away from the shelfbreak (Figures 16b, 16c, and 16f). When considering the contribution to the evolution of relative vorticity, the nonlinear advection term is also a significant contributor (Figures 16g versus 16c). This makes sense in that the movement of the WCR largely depends on the ambient circulation condition. The residual of APV and JEBAR, together with ADV dominate the change of relative vorticity of the WCR. The stress curl and dissipation terms (not shown) were much smaller during the period. We note that since the data assimilation performs sequential updates every 3 days, the evolution of the flow from 1 to 7 May is not completely consistent. The tendency computed from differencing the 1 to 7 May vorticity fields therefore needs not balance with other vorticity budget terms calculated on 4 May. Such residual is small however, as shown in Figure 16i.

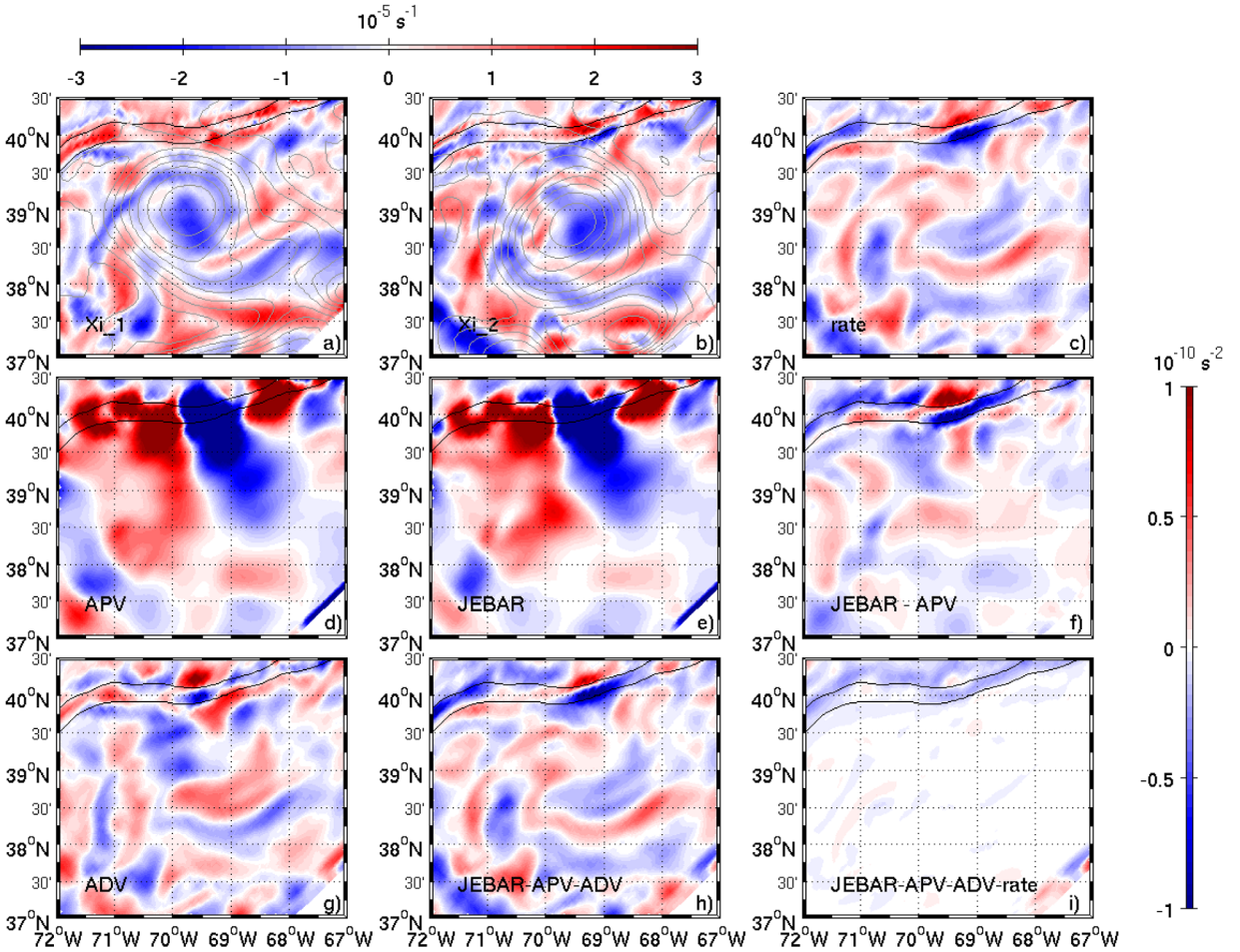

Figure 16. Depth-averaged relative vorticity with associated source and sink terms during the period when the WCR was impinging on the shelfbreak. (a, b) Depth-averaged relative vorticity on 1 and 7 May 2006, respectively, with values shown in the horizontal colorbar. Sea surface height is shown by gray contours. (c) Time rate of change of depth-averaged relative vorticity. (d) Advection of potential vorticity (APV). (e) Joint Effect of Baroclinicity and Bottom Relief (JEBAR). (f) Residual of JEBAR and APV. (g) Nonlinear advection of relative vorticity (ADV). (h) Total effect of JEBAR, APV, and ADV. (i) Residual of JEBAR, APV, ADV, and rate terms. All source and sink values are shown by the vertical colorbar. In each plot, the 200 and 1000 m isobaths are shown by the black curves.

5. Discussions and Summary

The WCR plays a key role in the water-mass/heat/salt exchange processes between the shelf-deep oceans around the Mid-Atlantic Bight. The reliable estimation of the mass/heat transports associated with the WCR has been a very challenging problem. Well-designed ocean general circulation models basically represent the WCR-shelf interaction processes without the data assimilation (e.g., Figure 2); however, representation of the exact location, size, and intensity of the WCR is vital for the quantitative estimation of the water-mass/heat/salt exchange processes. The present study solves the problem by effectively combining an eddy-resolving ocean general circulation model and various observation data using a state-of-the-art 4D-VAR data assimilation method. We focused on a large Gulf Stream Warm Core Ring event occurred in April–May 2006. Our MABGOM 4D-Var model assimilated mapped satellite surface height and surface temperature, in situ temperature and salinity data measured by CTD, XBT, and ARGO floats, as well as glider transect surveys. Through data assimilation, the model skill was significantly improved. The temporal and spatial evolutions of the WCR and its interaction with the shelf circulation were realistically reproduced.

In this study, the control variables adjusted by 4D-Var data assimilation include initial condition, lateral boundary condition, and surface forcing. We found that the adjustment of the initial condition is the most important in retaining the shape and intensity of the ring. The performance of data assimilation depends critically on the parameterization of the background error covariance matrix **B**. As a part of **B**, standard deviation errors of state variables were estimated based on intrinsic variability of the forward model [*Powell*

et al., 2008; *Broquet et al*., 2009; *Moore et al*., 2011b]. Thus, the performance of the forward model is important because the extent to which the standard deviation derived from the forward simulation represents the realistic variability will directly impact the cost function and increments distribution. In our application, we had to use the clamped open boundary conditions for 3-D momentum and tracer variables to ensure the exact correspondence in set up between the nonlinear model and tangent linear/adjoint model. We also implemented a narrow sponge layer around the open boundaries, within which we imposed tracer nudging back to HYCOM temperature and salinity fields to keep the strong western boundary current in its proper position. More model sensitivity experiments need to be carried out as the tangent linear/adjoint model adapts more open boundary condition options, which can potentially allow us to improve the error covariance function specification based on the forward simulations. Another element in building **B** is the choice of horizontal and vertical decorrelation scales of state variables. Based on the typical characteristics of WCR, we used 50 km and 30 m for horizontal and vertical decorrelation scales, respectively, in this study. More sensitivity experiments on these scale selection are needed in the future.

The observational error covariance **R** is another important element in the definition of the cost function and its minimization. If large observational errors are assigned, a relatively loose constraint is applied on model prediction, which may limit the model's ability in fitting observations. On the other hand, if observational errors are too small, they will likely exert a stronger than needed constraint on the model, resulting in excessive increments in control variables that could overperturb the ocean states and impair model performance. How to best define R is therefore an active area of research.

The length of the assimilation window needs to be optimal to guarantee tangent-linear approximation. We chose 3 day as the window for the assimilation. The Gulf Stream and its eddy system that we are targeting here are very nonlinear (with relative vorticity being >1 f), a longer assimilation window may impair the tangent-linear assumption used by the adjoint model. The choice was also based on experience and lessons learned from an earlier ROMS 4D-Var application on the New Jersey shelf. In that subregional shelf modeling setup, 3 day was also used as the assimilation window (personal communication with Modeling Group at Rutgers University, also see their online documentation at: http://www.myroms.org/applications/espresso/). We have performed sensitivity experiments using longer assimilation windows, and confirmed that 3 day window was a good choice to both effectively reduce model-data misfits and achieve smooth model trajectories at the same time.

The quality of data being assimilated also needs careful considerations. In our case, we excluded SSH data on the shallow ($<$200 m) shelf areas because errors of altimeter product in the shallow waters are known to be very large [e.g., *Wilkin et al*., 2008]. It is our experience as well that the gridded altimetry data can be used to represent the large-scale western boundary current correctly, but they are not suitable for inner and mid shelf circulation process studies due to large uncertainties in atmospheric and tidal corrections of altimetry data. However, the SSH data in the slope sea and Gulf Stream region still have larger impact on the posterior solutions comparing to SST data.

Despite all these difficulties and uncertainties, our study demonstrates the powerful utility of ROMS 4D-Var in simulating the Northeast U.S. coastal ocean circulation. The model skill is significantly improved via data assimilation. Over the entire 2 month study period, errors in SSH and SST are reduced by 79% and 65%, respectively (not shown). Significant model skill improvement is also evident when compared to subsurface observations. The good comparison with the independent ECOMON hydrographic data is particularly illustrative, showing the system's ability in refining the state variables in both observation and model spaces.

The motion of the large WCR in 2006 had a dramatic impact on the MAB shelf/slope circulation. The interaction between the WCR and the shelfbreak front and jet is in particular important because it controls cross-shelf exchanges of physical and biogeochemical material properties. Considering the vast differences at the leading and trailing edges of the WCR, we can compare the cross-shelf structure across the shelfbreak front. Transects of mean temperature, salinity, and along-shelf velocity were calculated for the WCR period from 22 April to 18 May at both edges of the WCR (Figure 17). Along the western transect (top), warm/saline WCR water dramatically altered the typical hydrographic features at this time of year [*Linder and Gawarkiewicz*, 1998; *Chen and He*, 2010]. The thermocline sloped downward moving offshore (Figure 17a). The impinging anticyclonic WCR led to a poleward movement of slope water and the shelfbreak jet was deflected further onshore (Figure 17c). In comparison, along the eastern transect on the trailing edge of the

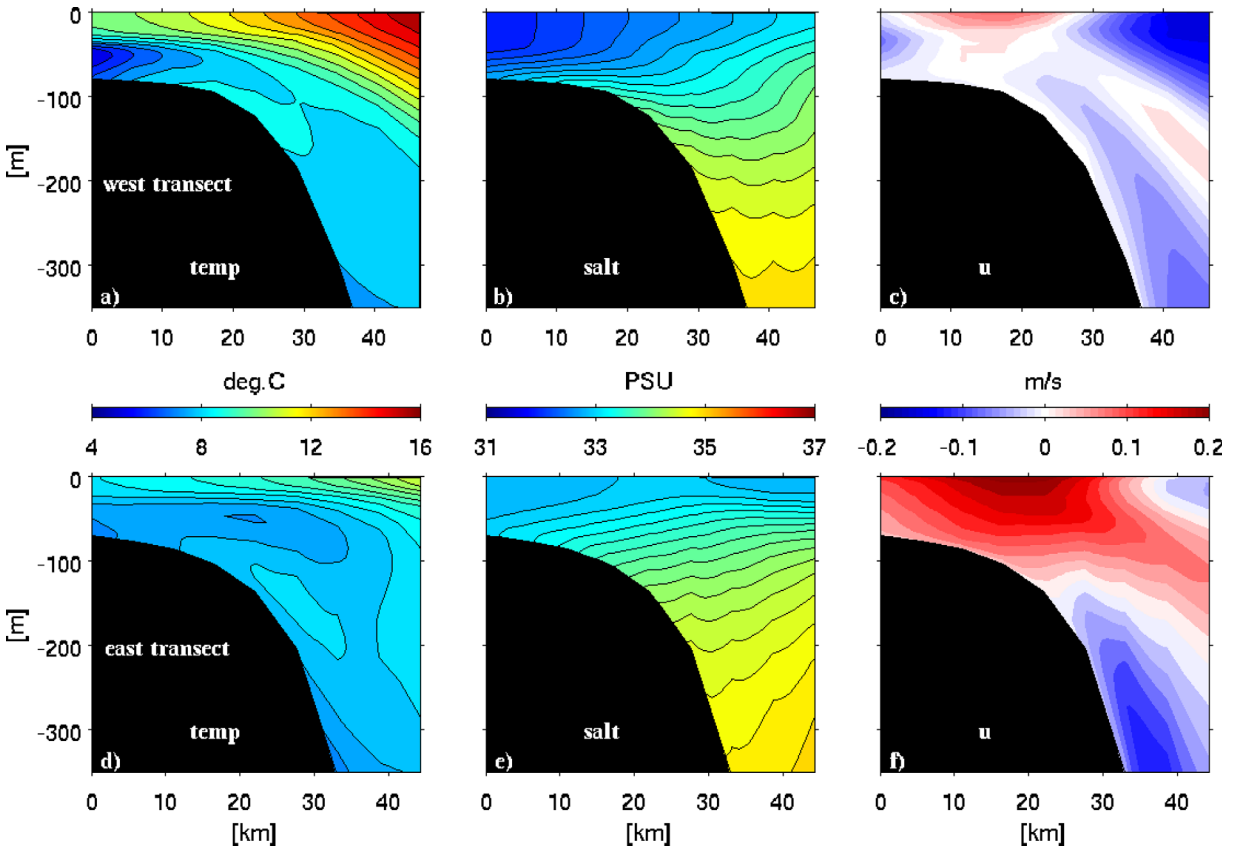

Figure 17. Cross-sectional view of mean (from 22 April to 18 May) temperature, salinity, along-shelf velocity (positive equatorward) along a western and eastern transect. The location of the transects are marked by the two black line segments in Figure 13.

WCR (bottom), due to the entrainment and offshore transport of shelf water, the hydrographic isosurfaces were flattened (Figures 17d and 17e). The most striking feature we note was the strong equatorward current on the shelf (Figure 17f), which was at least 40 km wide and extended from the surface to nearly 200 m at depth. The transport in the shelf waters was 0.36 Sv, which is comparable to the mean shelfbreak jet transport. Our results are consistent with *Gawarkiewicz et al*. (2001] in that the shelfbreak front was steeper at the leading flank of the WCR and the front is flatter at the trailing flank of the WCR. The impact of the WCR on the shelfbreak circulation extended far downstream. Off New Jersey an enhanced shelfbreak jet was present (maximum along-shelf velocity of 0.4 m s^{-1}) due to the enhanced cross-shelf gradients resulting from the intrusion of ring water.

A more complete picture of the impact of the WCR on the shelfbreak frontal circulation is depicted in Figure 18. Before the impingement of the WCR, we can see from the subsurface map that the shelfbreak jet was a continuous flow running along the shelfbreak. During the impingement of the WCR, the shelfbreak circulation was dramatically altered. On the leading edge, the shelfbreak front was pushed onshore and the shelfbreak jet weakened. On the trailing edge of the WCR, the shelfbreak jet was diverted offshore due to the offshore entrainment of shelf water, essentially resulting in a shutdown of the shelfbreak jet.

Entrainment of shelf water has been reported in earlier studies [e.g., *Morgan and Bishop*, 1977; *Garfield and Evans*, 1987]. The footprint of entrained shelf water is not well understood due to the limitations of available observations. Previous observations revealed the shelf water accumulates around the periphery of a WCR adjacent to the maximum azimuthal velocity, where the azimuthal velocity is decreasing [*Joyce*, 1984]. Recent laboratory experiments [*Cenedese et al*., 2013] show that the offshore extent of the streamer depends on the relative strength of the maximum WCR azimuthal velocity relative to the maximum velocity in the undisturbed shelfbreak jet. Our results show the entrained fresh water on the shelf extended offshore at a distance of the radius of the WCR, and may have reached as far offshore as the Gulf Stream northern

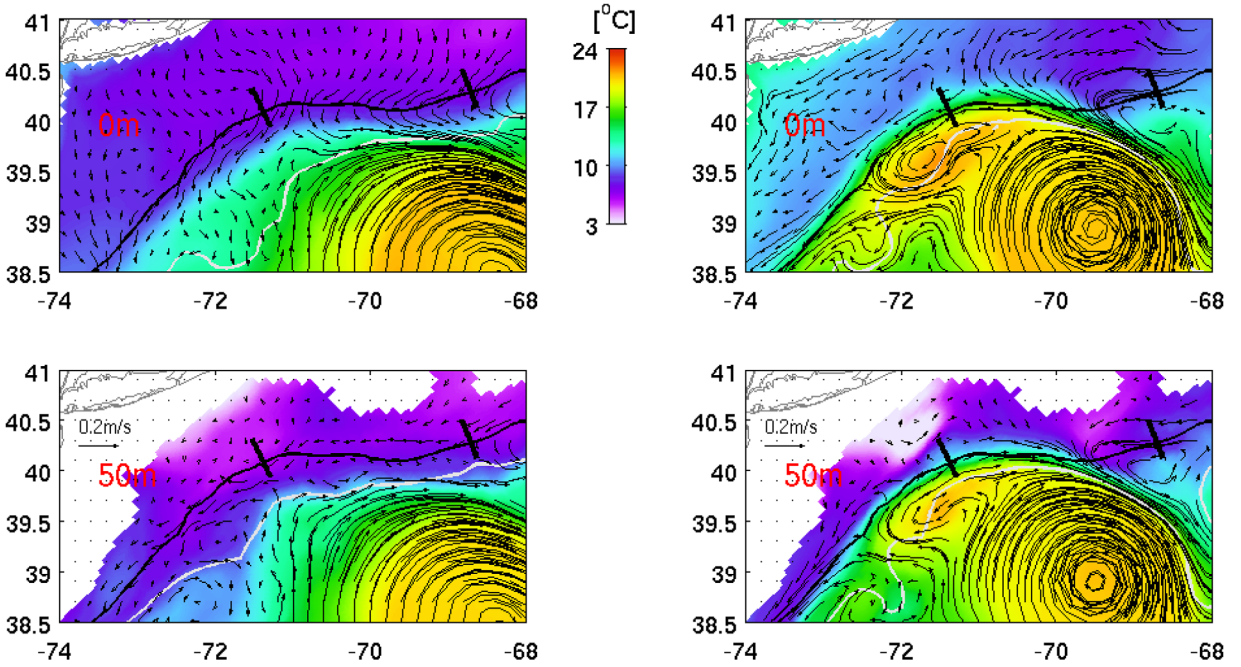

Figure 18. Mean temperature and velocity before WCR impingement (1–20 April, left plots) and during WCR impingement (1–7 May, right plots). Surface fields are shown in the first row while subsurface (50 m) fields are shown in the second row. Locations of the two transects in Figure 17 are also shown.

wall. We also note that after the detachment of the WCR from the Gulf Stream (and the cutoff of the supply of warm and saline Gulf Stream water to the WCR), the salinity near the center of the WCR was greatly decreased (Figure 11) as a result of entrainment of fresh shelf water. This is quite evident after the impingement of the WCR on the shelfbreak (Figure 12). Decreases in salinity within the WCR reduced the cross-shelf density gradient, and contributed to the spin-down of the WCR. The salinity in the core of the WCR did not increase again until the WCR reattached to the Gulf Stream (Figure 13).

In summary, using a state-of-the-art 4-dimensional variational data assimilation technique, we performed a data assimilative modeling study on a large Gulf Stream WCR occurred in spring 2006. This WCR was one of the largest and most energetic in recent decades. It had a life span of approximately 27 days, detaching on 22 April 2006 and reattaching back to the Gulf Stream again on 18 May 2006. The initial radius and depth of the WCR were estimated as 96 km and 1000 m, respectively. The WCR moved toward the continental shelf and made contact with the shelfbreak in early May. The largest impacts of the WCR on the shelfbreak lasted about 1 week and induced dramatic exchanges between shelf and slope waters. Mean cross-shelf transport of shelf water was estimated at 0.28 Sv during the impingement period, which is comparable to the total transport of the shelfbreak jet. The maximum offshore heat/salt flux was -8900 W m^{-2}/-4×10^{-4} kg m^{-2} s^{-1}, respectively on 3 May 2006. These values are about 6–9 times larger than the long-term mean values (1000 W m^{-2}/6.7×10^{-4} kg m^{-2} s^{-1}) [*Chen and He*, 2010]. During the evolution and spin-down process of the WCR, the radius and intensity of the ring were both reduced. The advection of potential vorticity and joint effect of baroclinicity and bottom relief (JEBAR) were the two largest terms in the vorticity budget while the variation of relative vorticity of the WCR was largely controlled by the nonlinear advection effect. The combination of baroclinicity and sloping bottom topography (JEBAR) generated depth-average transport across the shelf, and led to vorticity change around the periphery of the ring as the WCR moved away from the shelfbreak. The entrainment of fresh shelf water into the center of the WCR led to the decrease of radial density gradients within the ring, and subsequently contributed to the spin-down of the WCR. The WCR retreated back to the slope sea and eventually was absorbed by the Gulf Stream.

Our study shows that a single large WCR can significantly alter the annual mean cross-shelf transport of mass, heat and salt. Fundamentally, understanding and predicting MAB shelf/slope exchange processes

needs to resolve both the local frontal dynamics as well as eddy processes induced by the Gulf Stream and other deep-ocean forcing.

Acknowledgments
Research support provided through ONR grants N00014-06-1-0739, N00014-10-1-0367, and NSF grant OCE-0927470 is much appreciated. B. Powell was supported by ONR grant N00014-09-10939. K. Chen was supported by the Woods Hole Oceanographic Institution Postdoctoral Scholar Program. K. Chen and R. He thank W. G. Zhang for valuable discussions on the 4D-Var model implementation of this study.

References

Bisagni, J. (1983), Lagrangian current measurements within the eastern margin of a warm-core Gulf Stream ring, *J. Phys. Oceanogr.*, *13*(4), 709–715.
Bisagni, J. J., H.-S. Kim, and A. Chaudhuri (2009), Interannual variability of the shelf-slope front position between 75 and 50 W, *J. Mar. Syst.*, *78*, 337–350.
Broquet, G., C. A. Edwards, A. M. Moore, B. S. Powell, M. Veneziani, and J. D. Doyle (2009), Application of 4D-variational data assimilation to the California Current System, *Dyn. Atmos. Oceans*, *48*, 69–92.
Broquet, G., A. M. Moore, H. G. Arango, and C. A. Edwards (2011), Corrections to ocean surface forcing in the California Current System using 4D variational data assimilation, *Ocean Modell.*, *36*, 116–132.
Cane, M. A., V. M. Kamenkovich, and A. Krupitsky (1998), On the utility and disutility of JEBAR, *J. Phys. Oceanogr.*, *28*, 519–526.
Castelao, R. M., S. Glen, R. Chant, and J. Kohut (2008), Seasonal evolution of hydrographic fields in the central Middle Atlantic Bight from glider observations, *Geophys. Res. Lett.*, *35*, L03617, doi:10.1029/2007GL032335.
Cenedese, C., R. E. Todd, G. G. Gawarkiewicz, W. B. Owens, and A. Y. Shcherbina (2013), Offshore transport of shelf waters through interaction of vortices with a shelfbreak current, *J. Phys. Oceanogr.*, *43*(5), 905–919.
Chapman, D. C., and K. H. Brink (1987), Shelf and slope circulation induced by fluctuating offshore forcing, *J. Geophys. Res.*, *92*(C11), 11,741–11,759, doi:10.1029/JC092iC11p11741.
Chassignet, E. P., H. E. Hurlburt, O. M. Smedstad, G. R. Halliwell, P. J. Hogan, A. J. Wallcraft, R. Baraille, and R. Bleck (2006), The HYCOM (HYbrid Coordinate Ocean Model) data assimilative system, *J. Mar. Syst.*, *65*(1–4), 60–83.
Chaudhuri, A., J. Bisagni, and A. Gangopadhyay (2008), Shelf water entrainment by Gulf Stream warm-core rings between 75°W and 50°W during 1978–1999, *Cont. Shelf Res.*, *29*, 393–406.
Chen, K. (2011), *Middle Atlantic bight shelfbreak circulation dynamics and biophysical interactions, PhD thesis*, N. C. State Univ., Raleigh.
Chen, K., and R. He (2010), Numerical investigation of the middle Atlantic bight shelfbreak frontal circulation using a high resolution ocean hindcast model, *J. Phys. Oceanogr.*, *40*, 949–964.
Churchill, J. H., P. C. Cornillon, and G. W. Milkowski (1986), A cyclonic eddy and shelf-slope exchange associated with a Gulf Stream warm-core ring, *J. Geophys. Res.*, 91(C8), 9615–9623, doi:10.1029/JC091iC08p09615.
Courtier, P., J. N. Thépaut, and A. Hollingsworth (1994), A strategy for operational implementation of 4D-Var, using an incremental approach, *Q. J. R. Meteorol. Soc.*, *120*(519), 1367–1387.
Curry, R. (2001), *A Database of Hydrographic Profiles and Tools for Climatological Analysis*, pp. 81, Woods Hole Oceanogr. Inst., Woods Hole.
Derber, J., and A. Rosati (1989), A global oceanic data assimilation system, *J. Phys. Oceanogr.*, *19*, 1333–1347.
Di Lorenzo, E., A. M. Moore, H. G. Arango, B. D. Cornuelle, A. J. Miller, B. Powell, B. S. Chua, and A. F. Bennett (2007), Weak and strong constraint data assimilation in the inverse Regional Ocean Modeling System (ROMS): Development and application for a baroclinic coastal upwelling system, *Ocean Modell.*, *16*(3–4), 160–187.
Fairall, C. W., E. F. Bradley, J. E. Hare, A. A. Garchev, and J. Edson (2003), Bulk parameterization of air-sea fluxes: Updates and verification for the COARE algorithm, *J. Clim.*, *16*, 571–591.
Fisher, A. (1972), Entrainment of shelf water by the Gulf Stream northeast of Cape Hatteras, *J. Comput. Phys.*, *77*, 3248–3255.
Fisher, M. (1998), Minimization algorithms for variational data assimilation, in *Proceedings of the ECMWF Seminar on Recent Development in Numerical Methods for Atmospheric Modelling*, pp. 364–385, European Centre for Medium-Range Weather Forecasts, Reading, U. K.
Flather, R. A. (1976), A tidal model of the northwest European continental shelf, *Mem. Soc. R. Sci. Liege*, *6*(10), 141–164.
Ford, W., J. Longard, and R. Banks (1952), On the nature, occurrence and origin of cold, low salinity water along the edge of the Gulf Stream, *J. Mar. Res.*, *11*, 281–293.
Fratantoni, P. S., R. S. Pickart, D. J. Torres, and A. Scotti (2001), Mean structure and dynamics of the shelfbreak jet in the middle Atlantic bight during fall and winter, *J. Phys. Oceanogr.*, *31*, 2135–2156.
Garfield, N., and D. L. Evans (1987), Shelf water entrainment by Gulf Stream warm-core rings, *J. Geophys. Res.*, *92* (C12), 13,003–13,012, doi: 10.1029/JC092iC12p13003.
Garvine, R. W., K.-C. Wong, and G. G. Gawarkiewicz (1989), Quantitative properties of shelfbreak eddies, *J. Geophys. Res.*, *94*(C10), 14,475–14,483, doi:10.1029/JC093iC12p15593.
Gawarkiewicz, G., and C. A. Linder (2006), Lagrangian flow patterns north of Cape Hatteras using near-surface drifters, *Prog. Oceanogr.*, *70*(2–4), 181–195.
Gawarkiewicz, G., T. Fredelman, T. Church, and G. Luther (1996), Shelfbreak frontal structure on the continental shelf north of Cape Hatteras, *Cont. Shelf Res.*, *16*, 1751–1773.
Gawarkiewicz, G., F. Bahr, R. C. Beardsley, and K. H. Brink (2001), Interaction of a slope eddy with the shelfbreak front in the Middle Atlantic Bight, *J. Phys. Oceanogr.*, *31*, 2783–2796.
Gawarkiewicz, G., K. Brink, F. Bahr, R. Beardsley, and M. Caruso (2004), A large-amplitude meander of the shelfbreak front during summer south of New England: Observations from the Shelfbreak PRIMER experiment, *J. Geophys. Res.*, *109*, C03006, doi:10.1029/2002JC001468.
Guo, X., H. Hukuda, Y. Miyazawa, and T. Ymagata (2003), A triply nested ocean model for simulating the Kuroshio: Roles of horizontal resolution on JEBAR, *J. Phys. Oceanogr.*, *33*, 145–169.
Haidvogel, D. B., et al. (2008), Ocean forecasting in terrain-following coordinates: Formulation and skill assessment of the Regional Ocean Modeling System, *J. Comput. Phys.*, *227*, 3595–3624.
He, R., and R. Weisberg (2003), A loop current intrusion case study on the West Florida shelf, *J. Phys. Oceanogr.*, *33*, 465–477.
Houghton, R. W., D. B. Olson, and P. J. Celone (1986), Observation of an anticyclonic eddy near the continental shelfbreak south of New England, *J. Phys. Oceanogr.*, *16*, 60–71.
Ingleby, B., and M. Huddleston (2007), Quality control of ocean temperature and salinity profiles: Historical and real-time data, *J. Mar. Syst.*, *65*, 158–175.
Joyce, T. M. (1984), Velocity and hydrographic structure of a Gulf Stream warm-core ring, *J. Phys. Oceanogr.*, *14*, 936–947.
Joyce, T. M., J. K. B. Bishop, and O. B. Brown (1992), Observation of offshore shelf-water transport induced by a warm-core ring, *Deep Sea Res.*, *39*, S97–S113.

Joyce, T. M., C. Deser, and M. A. Spall (2000), The relation between decadal variability of Subtropical Mode Water and the North Atlantic Oscillation, *J. Clim.*, *13*, 2550–2569.
Le Traon, P.-Y., and G. Dibarboure (1999), Mesoscale mapping capabilities of multi-satellite altimeter missions, *J. Atmos. Oceanic Technol.*, *16*, 1208–1223.
Linder, C., and G. Gawarkiewicz (1998), A climatology of the shelfbreak front in the Middle Atlantic Bight, *J. Geophys. Res.*, *103*(C9), 18,405–18,423, doi:10.1029/98JC01438.
Loder, J. W., B. Petrie, and G. Gawarkiewicz (1998), The coastal ocean off northeastern North America: A large-scale view, in *The Sea*, pp. 105–133, John Wiley, New York.
Matthews, D., B. S. Powell, and I. Janekovic (2012), Analysis of four-dimensional variational state estimation of the Hawaiian waters, *J. Geophys. Res.*, *117*, C03013, doi:10.1029/2011JC007575.
Mellor, G. L., and T. Yamada (1982), Development of a turbulence closure model for geophysical fluid problems, *Rev. Geophys.*, *20*(4), 851–875.
Mertz, G., and D. G. Wright (1992), Interpretation of the JEBAR Term, *J. Phys. Oceanogr.*, *22*, 301–305.
Moore, A. M., H. G. Arango, E. D. Lorenzo, B. D. Cornuelle, A. J. Miller, and D. J. Neilson (2004), A comprehensive ocean prediction and analysis system based on the tangent linear and adjoint of a regional ocean model, *Ocean Modell.*, *7*, 227–258.
Moore, A. M., H. G. Arango, G. Broquet, C. Edwards, M. Veneziani, B. Powell, D. Foley, J. D. Doyle, D. Costa, and P. Robinson (2011a), The Regional Ocean Modeling System (ROMS) 4-dimensional variational data assimilation systems. Part III: Observation impact and observation sensitivity in the California Current System, *Prog. Oceanogr.*, *91*, 74–94.
Moore, A. M., H. G. Arango, G. Broquet, C. Edwards, M. Veneziani, B. Powell, D. Foley, J. D. Doyle, D. Costa, and P. Robinson (2011b), The Regional Ocean Modeling System (ROMS) 4-dimensional variational data assimilation systems. Part 2: Performance and application to the California Current System, *Prog. Oceanogr.*, *91*, 50–73.
Moore, A. M., H. G. Arango, G. Broquet, B. Powell, A. T. Weaver, and J. Zavala-Garay (2011c), The Regional Ocean Modeling System (ROMS) 4-dimensional variational data assimilation systems. Part 1: System overview and formulation, *Prog. Oceanogr.*, *91*, 34–49.
Morgan, C. W., and J. M. Bishop (1977), An example of Gulf Stream eddy-induced water exchange in the Mid-Atlantic Bight, *J. Phys. Oceanogr.*, *7*, 472–479.
Pascual, A., Y. Faugere, G. Larnicol, and P.-Y. L. Traon (2006), Improved description of the ocean mesoscale variability by combining four satellite altimeters, *Geophys. Res. Lett.*, *33*, L02611, doi:10.1029/2005GL024633.
Pickart, R. S., D. J. Torres, T. K. McKee, M. J. Caruso, and J. E. Przystup (1999), Diagnosing a meander of the shelfbreak current in the Middle Atlantic Bight, *J. Geophys. Res.*, *104*(C2), 3121–3132, doi:10.1029/1998JC900066.
Powell, B. S., H. Arango, A. M. Moore, E. D. Lorzenzo, and D. F. R. F. Milliff (2008), 4DVAR data assimilation in the Intra-Americas Sea with the Regional Ocean Modeling System (ROMS), *Ocean Modell.*, *25*, 173–188.
Powell, B. S., A. M. Moore, H. G. Arango, E. D. Lorenzo, R. F. Milliff, and R. R. Leben (2009), Near real-time ocean circulation assimilation and prediction in the Intra-Americas Sea with ROMS, *Dyn. Atmos. Oceans*, *48*, 46–68.
Ramp, S. R., R. C. Beardsley, and R. Legeckis (1983), An observation of frontal wave development on a shelf-slope/warm core ring front near the shelfbreak south of New England, *J. Phys. Oceanogr.*, *13*, 907–912.
Sarkisyan, A. S. (2006), Forty years of JEBAR: The finding of the joint effect of baroclinicity and bottom relief for the modeling of ocean climatic characteristics, *Izv. Atmos. Oceanic Phys.*, *42*(5), 534–554.
Sarkisyan, A. S., and V. F. Ivanov (1971), Joint effect of baroclinicity and bottom relief as an important factor in the dynamics of sea currents, Izv. Acad. Sci. USSR Atmos. *Oceanic Phys., Engl. Transl.*, no. 7, 173–178.
Shchepetkin, A. F., and J. C. McWilliams (2005), The regional oceanic modeling system (ROMS): A split-explicit, free surface, topography-following-coordinate oceanic model, *Ocean Modell.*, *9*, 347–404.
Taylor, K. E. (2001), Summarizing multiple aspects of model performance in a single diagram, *J. Geophys. Res.*, *106*(D7), 7183–7192, doi: 10.1029/2000JD900719.
Wang, X. (1992), *Interaction of an Eddy With a Continental Slope*, MIT Press, Cambridge, Mass.
Weaver, A. T., and P. Courtier (2001), Correlation modelling on the sphere using a generalized diffusion equation, *Q. J. R. Meteorol. Soc.*, *127*, 1815–1846.
Weaver, A. T., J. Vialard, and D. L. T. Anderson (2003), Three- and four-dimensional variational data assimilation with a general circulation model of the tropical Pacific Ocean. Part1: Formulation, internal diagnostics, and consistency checks, *Mon. Weather Rev.*, *131*, 1360–1378.
Wei, J., and D.-P. Wang (2009), A 3-dimensional model study of warm core ring interaction with continental shelf and slope, *Cont. Shelf Res.*, *29*, 1635–1642.
Wilkin, J., J. Zavala-Garay, J. Levin, and W. G. Zhang (2008), Four-dimensional variational assimilation of satellite temperature and sea level data in the coastal ocean and adjacent deep sea, in *IEEE International Symposium 2008 (IGARSS 2008) on Geoscience and Remote Sensing*, pp. III-427–III-430, IEEE Geoscience and Remote Sensing Society, Boston, Mass.
Zhang, W., J. Wilkin, and H. Arango (2010), Towards building an integrated observation and modeling system in the New York Bight using variational methods. Part I: 4DVAR data assimilation, *Ocean Modell.*, *35*, 119–133.